Joint Inversion

of Acoustic and Electromagnetic Wave Fields for Subsurface Imaging

Eva M. L. Scherders

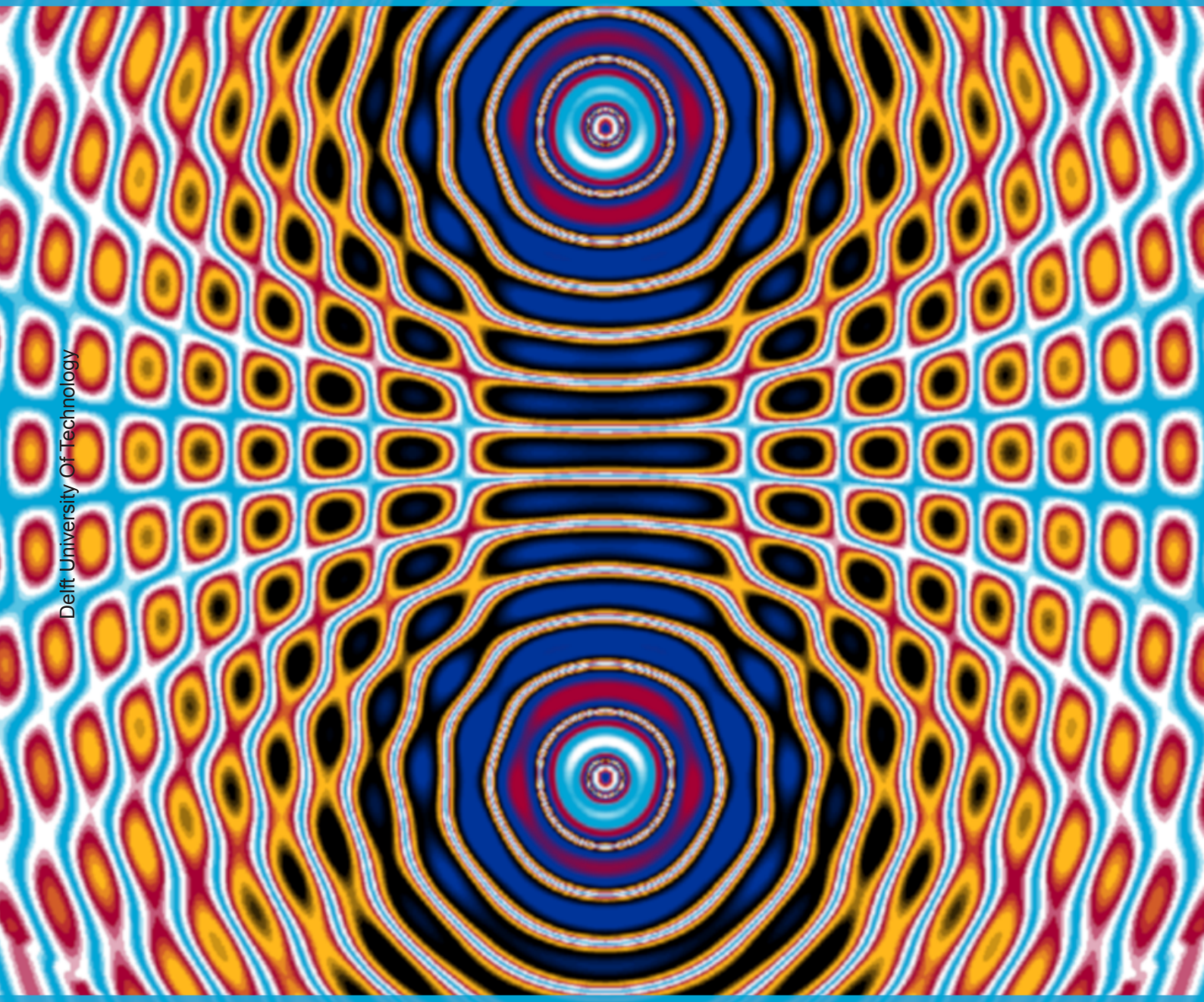

Delft University Of Technology

TU Delft

Joint Inversion

of Acoustic and Electromagnetic Wave Fields for Subsurface Imaging

by

Eva M. L. Scherders

to obtain the degree of Master of Science
at the Delft University of Technology,
to be defended publicly on Friday June 17, 2022 at 14:30 PM.

Student number:	4570731	
Project duration:	September 1, 2021 – June 1, 2022	
Thesis committee:	Dr. K. W. A. van Dongen,	TU Delft, supervisor
	Dr. D. J. Verschuur,	TU Delft
	Prof. dr. S. Stallinga,	TU Delft

TU Delft

Acknowledgements

A project is never completed completely alone. Therefore I would like to take this opportunity to thank the people without whom I never would have been able to complete my master thesis.

First of all I would like to thank my supervisor, Koen van Dongen, for his guidance throughout the project. I am grateful for the honest, personal involvement, which has empowered me to complete the project without any major problems. Thank you for being understanding and flexible, but at the same time trusting me with different types of responsibilities. It was a pleasure to have a supervisor who thinks in opportunities rather than problems, an inspiring environment to learn in.

From the research group computational imaging, I would like to thank everybody who has taken the time to listen to my progress presentation and share ideas on the topic. The involvement of people working on completely different types of projects has yielded interesting point of views.

Next, I would like to give some special attention to my buddy in the student room of the computational imaging department: Enya Berrevoets. I have truely enjoyed our lunches together, typically involving inspiring political, philosophical or psychological discussions. On top of that, it was great to have someone who was dealing with similar situations, and being able to talk each other through struggles where necessary.

Finally I would like to thank the people close to me, for listening, relativizing and making me laugh when I got stuck during the project. In particular, these people are my roommates, Fé, Floor, Ilva, Josien, Silvy and Veerle, my parents and finally, and most importantly Jasper. Thank you!

Eva M. L. Scherders
Delft, June 2022

Abstract

Imaging by inversion of acoustic or electromagnetic wave fields have applications in a wide variety of areas, such as non-destructive testing, biomedical applications, and geophysical explorations. Unfortunately, each modality suffers from its own application specific limitations, typically being difficulties in distinguishing different materials or tissues from each other in the case of acoustic wave fields and a low spatial resolution in the case of electromagnetic wave fields. To exploit the advantages of both imaging modalities, methods to combine them include image fusion, usage of spatial priors and application of joint or multi-physics inversion methods. The latter can be based on empirical relations between acoustic and electromagnetic medium properties or on structural similarity. In this work, two joint inversion algorithms based on structural similarity are presented. To account for the structural similarity the error-functional of standard Born inversion is extended with an additional penalty term. This additional term is either based on the L2-norm of the cross-gradient (CG), i.e. the cross product of the gradients of the acoustic and electromagnetic contrasts or on the L2-norm of the gradient difference (GD), i.e. the difference between the normalized gradients of both contrasts. To test the proposed methods, two synthetic models are considered; one with the gradients of the contrasts pointing in the same direction and one where the gradients point in opposite directions. Results show that the GD constraint significantly improves the resolution for the electromagnetic reconstruction compared to separate BI. The mean square errors (MSE) of the reconstructed profiles for the separate BI are 0.12 for the acoustic and 0.51 for the electromagnetic case, and for the joint GD inversion, 0.09 for the acoustic and 0.46 for the electromagnetic case. The joint GD inversion fails when using the model with the gradients of the contrasts pointing in opposite directions. The joint CG inversion does not enhance the reconstructed images, but shows similar performances for the different models. In conclusion, joint inversion based on structural constraints is shown to improve the electromagnetic resolution, especially using the GD constraint. Further research needs to be conducted to extend the functionality of the GD constraint to acoustic and electromagnetic contrasts with opposite contrast gradient directions.

Contents

1

Introduction

Imaging by inverse scattering of acoustic waves is used in a variety of fields, like non-destructive testing of for example art objects [1], biomedical applications like breast imaging [2], remote sensing [3] and geophysical explorations [4]. Correspondingly, imaging by inverse scattering of electromagnetic waves also has wide applications in the same fields [5–9], although both modalities generally suffer from their own application specific disadvantages. For example, in hydrocarbon explorations, seismic or acoustic data inversion is unsuccessful in differentiating areas filled with water from hydrocarbons, due to the low contrast in acoustic velocities between these fluids [10]. On the other hand, electromagnetic data has the disadvantage of exhibiting a much lower resolution than the acoustic data due to its diffusive nature [11], as well as the difficulty in distinguishing gas-filled regions from oil-filled regions [10]. Also in breast cancer imaging the heterogeneous tissue causes low resolution and low localization accuracy, when using long wavelength electromagnetic waves [12]. In contrast, acoustic imaging provides a high resolution [2], but shows low contrast in speed of sound between malignant and healthy tissue [13], where there is a high contrast between these tissues in electromagnetic parameters [6].

In order to exploit the advantages of both imaging modalities, several strategies to combine them have been proposed in the last decades. Firstly, for combining ultrasound imaging with other imaging modalities in biomedical applications, image fusion is commonly applied [14]. Here, images are collected separately and combined afterwards. One step further is the technique of model fusion, or the use of spatial priors [12, 15–19]. In this approach structural information is derived from ultrasound images and is incorporated as regularization term in the inversion process of the electromagnetic or microwave image. Several methods have been proposed to use this information. The first method is to extract regions from the ultrasound image, and assign a priori electromagnetic parameters, such as the electric permittivity, to these regions, that are included as an inhomogeneous background during inversion [12, 15]. Another method is to use a regularization in the inversion process that favours similarity of the permittivity within the a priori defined regions [16], or favours similarity of the permittivity of neighbouring pixels that do not lie on an edge [16, 17]. A different approach is given in [19], where the authors use a fuzzy C-means clustering to identify the background of the image, which is used as input for the electromagnetic image. Lastly, a convolutional neural network can be applied to predict the permittivity distribution, which can be used as prior information in the microwave inversion process [18].

All these methods include high resolution prior information into the inversion of electromagnetic waves to improve the resulting reconstruction as compared to separate, sequential inversion. However, the authors of [17] suggest that a better exploitation of this prior information could be preferable. A method that combines acoustic and electromagnetic imaging in an even stronger manner by constraining both imaging modalities with the other is called joint inversion or multi-parameter inversion and will be the subject of this master thesis. The joint inversion algorithms are extended from widely used separate inversion algorithms, which include the Born iterative method (BIM) [20], the distort BIM (DBIM) [21], the variational BIM (VBIM) [22], Born inversion (BI) [23], contrast source inversion (CSI) [24] and subspace-based optimization method (SOM) [25].

In literature, three methods of joint inversion have been investigated; joint inversion based on empirical relationships between the imaged parameters, based on mutual information and based on structural similarity [26]. The former method is mostly investigated in geophysics [11,27–31], where petrophysical links between seismic velocities and electromagnetic resistivity are used. This is for example done by linking seismic velocities to water saturation and porosity through Archie's equation [32], and resistivity to water saturation and porosity through Gassmann's fluid-substitution equations [33]. Despite being a strong constraint, the choice of petrophysical parameters is problem dependent, and the errors in these parameters will easily propagate into the results [31]. The petrophysical joint inversion approach is therefore very effective, if there is good a priori knowledge of the problem specific petrophysical relationships [29]. In biomedical applications these relationships are less straightforward [34].

The second joint inversion method, joint inversion based on mutual information, is based on theoretical properties and therefore intuitive. However the technique is highly non-linear due to the use of the probability density function [34]. In [26], no tests converged as local minima could not be avoided. The last method, joint inversion based on structural similarity has also been first employed in geophysics [35]. Here, a similarity between the distribution of physical parameters is assumed and is incorporated as a regularization term in the cost function.

Structural similarity is defined by [26] as the level sets of two functions, the contours or surfaces where the functions are constant, being parallel to each other. An even stronger definition is that the level sets should not only be parallel, but should located at the same positions. A measure for structural similarity is given in [35] as the magnitude of the Laplacian operator and two thresholds. Another approach is the use of the cross product of the gradients of the two images, or short the cross gradient function. This method is widely explored in geophysics [10, 26, 31, 36–40], but also in the biomedical context [41–43] and was first suggested by [36]. The cross-gradient function vanishes if the gradients in the acoustic and electromagnetic image are in the same direction, irrespective of their sign. On top of that, if in one image there is no structure, the gradient is zero and the structure present in the other image is not enforced. A slightly different variant of the cross-gradient is the normalized cross-gradient function [39]. Normalizing the cross-gradient function removes the dominance of rapidly varying functions which normally occur in the subsurface of the earth compared to deeper regions [39]. A problem with the normalized cross-gradient function is that when discretized, very small gradients can result in arbitrarily large cross-gradients. Consequently, the inversion can focus primarily on minimizing these large cross-gradients. Apart from the Laplacian and the cross-gradient function, the authors of [34, 44] have used a different method to imply structural similarity, by letting the magnitude of the gradients constrain each other in interactive regularization terms. In [13], edge preserving regularization is used, where hidden variables indicate the parameter discontinuities in different directions. These hidden variables are updated alternatively with the contrasts of both wave fields. Finally, [41] proposes an approach to use the difference between the gradients of the acoustic and electromagnetic contrasts as the joint structural constraint, where promising results are found, but no tests on contrasts with opposite gradient signs have been conducted.

In this master thesis, two joint inversion algorithms using acoustic and electromagnetic waves based on structural similarity are developed in Fortran. They serve as the framework of future research in this field, in continuation of the work in [41]. Both the cross-gradient and the gradient difference constraint are implemented as regularization to couple both imaging modalities, and the cost-function will be minimized in an alternating fashion. The inversion is executed using BI and CSI for the separate case and BI for the joint inversions, from which the results are compared. The underlying theory is introduced in Chapter 2, next the method is presented in Chapter 3. Chapter 4 includes the inversion results, followed by a discussion in Chapter 5 and finally, the conclusions are given in Chapter 6.

2

Theory

This chapter provides an overview of the theory used within this thesis. First the theory behind the acoustic and electromagnetic wave fields are discussed in Section 2.1, followed by a section on solution methods.

2.1. Wave fields

In joint inversion, data from reflected acoustic and electromagnetic wave fields is used to reconstruct the physical properties of the imaged structure. The wave equations and properties of both wave fields are discussed in the following two subsections.

2.1.1. Acoustic wave fields

Acoustic time-harmonic waves can be described by a spatially fluctuating scalar pressure field and a spatially fluctuating vectorial velocity field of the particles of the medium. The pressure field and the velocity field are described by Hooke's law and Newton's law respectively and are given by

$$\frac{\partial p(\vec{r},t)}{\partial t} = -\frac{1}{\kappa(\vec{r})}\nabla\cdot\vec{v}(\vec{r},t) + \frac{1}{\kappa(\vec{r})}q(\vec{r},t), \tag{2.1}$$

$$\nabla p(\vec{r},t) = -\rho_0\frac{\partial\vec{v}(\vec{r},t)}{\partial t} + \vec{f}(\vec{r},t), \tag{2.2}$$

where, $p(\vec{r},t)$ is the pressure field, $\vec{v}(\vec{r},t)$ the velocity field, $\kappa(\vec{r})$ the compressability of the medium, ρ_0 the assumed constant mass density of the medium, $q(\vec{r},t)$ the volume source density of injection rate, $\vec{f}(\vec{r},t)$ the volume source density of volume force, $\vec{r}$ the coordinate vector and t the time.

Combining equation (2.1) and (2.2) gives the acoustic wave equation for heterogeneous media,

$$\nabla^2 p(\vec{r},t) - \frac{1}{c_{A,0}^2}\frac{\partial^2 p(\vec{r},t)}{\partial t^2} = -S_A^{pr}(\vec{r},t) + \chi_A(\vec{r})\frac{\partial^2 p(\vec{r},t)}{\partial t^2}. \tag{2.3}$$

Transforming (2.3) to the temporal Fourier domain with angular frequency, ω, yields,

$$\nabla^2\hat{p}(\vec{r}) + \frac{\omega^2}{c_{A,0}^2}\hat{p}(\vec{r}) = -\hat{S}_A^{pr}(\vec{r}) - \omega^2\chi_A(\vec{r})\hat{p}(\vec{r}), \tag{2.4}$$

where $\hat{p}(\vec{r}) = \int_{-\infty}^{\infty} p(\vec{r},t)e^{i\omega t}dt$ is used as the definition for the Fourier transform, $\hat{S}_A^{pr}(\vec{r})$ is the primary source term of the acoustic field given by $\hat{S}_A^{pr}(\vec{r}) = i\omega\rho_0\hat{q}(\vec{r}) - \nabla\vec{\hat{f}}(\vec{r})$, $\chi_A(\vec{r})$ the acoustic contrast of the medium given by

$$\chi_A(\vec{r}) = \frac{1}{c_A^2(\vec{r})} - \frac{1}{c_{A,0}^2}, \tag{2.5}$$

with $c_A(\vec{r})$ the speed of sound at position $\vec{r}$, and $c_{A,0}$ the speed of sound of the homogeneous background medium. These speed of sounds are defined by $c_A^{-2}(\vec{r}) = \rho_0\kappa(\vec{r})$ and $c_{A,0}^{-2} = \rho_0\kappa_0$, respectively. The last term in equation (2.4) can also be regarded as an extra source term, called the acoustic contrast source, that equals $\hat{w}_A(\vec{r}) = \chi_A(\vec{r})\hat{p}(\vec{r})$. Note that from equation (2.4) and onward the caret symbol, ^, is used to denote quantities defined in the temporal Fourier domain.

Equation (2.4) can be recasted into an integral equation of the second kind. Within this formulation the pressure field is written as a superposition of the incident field, $\hat{p}^{inc}(\vec{r})$ induced by the primary source term and propagating in the homogeneous background medium and the scattered field, $\hat{p}^{sct}(\vec{r})$, induced by the contrast source term, hence

$$\hat{p}(\vec{r}) = \hat{p}^{inc}(\vec{r}) + \hat{p}^{sct}(\vec{r}). \tag{2.6}$$

The incident field is obtained by the convolution of the impulse response function of the homogeneous background medium, the Green's function $\hat{G}_A(\vec{r} - \vec{r}')$, with the primary source, hence

$$\hat{p}^{inc}(\vec{r}) = \int_{\vec{r}' \in \mathbb{S}} \hat{G}_A(\vec{r} - \vec{r}')\hat{S}_A^{pr}(\vec{r}')dV(\vec{r}'). \tag{2.7}$$

Similarly, the scattered field can be described by the convolution of the Green's function with the contrast source term,

$$\hat{p}^{sct}(\vec{r}) = \omega^2 \int_{\vec{r}' \in \mathbb{D}} \hat{G}_A(\vec{r} - \vec{r}')\hat{w}_A(\vec{r}')dV(\vec{r}') = \omega^2 \int_{\vec{r}' \in \mathbb{D}} \hat{G}_A(\vec{r} - \vec{r}')\chi_A(\vec{r}')\hat{p}(\vec{r}')dV(\vec{r}'). \tag{2.8}$$

In equations (2.7) and (2.8), $\mathbb{S}$ represents the spatial domain where the sources and the receivers are placed, and $\mathbb{D}$ the domain of interest. In 2-D, the volume integrals in equations (2.7) and (2.8) reduce to surface integrals. The Green's functions of the 2-D and 3-D case are respectively,

$$\hat{G}_A^{2D}(\vec{r} - \vec{r}') = \frac{-i}{4}H_0^{(2)}(\omega|\vec{r} - \vec{r}'|/c_{A,0}), \tag{2.9}$$

$$\hat{G}_A^{3D}(\vec{r} - \vec{r}') = \frac{e^{-i\omega|\vec{r}-\vec{r}'|/c_{A,0}}}{4\pi|\vec{r} - \vec{r}'|}, \tag{2.10}$$

where $H_0^{(2)}(\omega|\vec{r} - \vec{r}'|/c_{A,0})$ is the Hankel function of the second kind. A derivation of these functions can be found in Appendix A, [45–48].

2.1.2. Electromagnetic wave fields

The wave equation for electromagnetic time-harmonic waves in lossless (conductivity, σ = 0 $\mathrm{S/m}$), heterogeneous media can be derived from Maxwell's equations,

$$\nabla \times \vec{E}(\vec{r}, t) = -\mu_0 \frac{\partial \vec{H}(\vec{r}, t)}{\partial t}, \tag{2.11}$$

$$\nabla \times \vec{H}(\vec{r}, t) = \epsilon(\vec{r}) \frac{\partial \vec{E}(\vec{r}, t)}{\partial t} + \vec{J}^{pr}(\vec{r}, t), \tag{2.12}$$

$$\nabla \cdot \Big[\epsilon(\vec{r})\vec{E}(\vec{r}, t)\Big] = \rho_e^{pr}(\vec{r}, t) = 0, \tag{2.13}$$

$$\nabla \cdot \Big[\mu_0\vec{H}(\vec{r}, t)\Big] = 0, \tag{2.14}$$

where, $\vec{E}(\vec{r}, t)$ is the electric field, $\vec{H}(\vec{r}, t)$ the magnetic field, $\vec{J}^{pr}(\vec{r}, t)$ the primary electric current density, $\rho_e^{pr}(\vec{r}, t)$ the primary electric charge density source, μ_0 the assumed constant permeability of the medium and $\epsilon(\vec{r})$ the electric permittivity of the medium.

Combining equations (2.11) - (2.14) and using the vector calculus identity $\nabla \times (\nabla \times \vec{A}) = \nabla(\nabla \cdot \vec{A}) - \nabla^2\vec{A}$, yields the wave equation for electromagnetic waves in lossless, heterogeneous media,

$$\nabla^2\vec{E}(\vec{r}, t) - \frac{1}{c_{E,0}^2}\frac{\partial^2\vec{E}(\vec{r}, t)}{\partial t^2} = -\vec{S}_E^{pr}(\vec{r}, t) + \chi_E(\vec{r})\frac{\partial^2\vec{E}(\vec{r}, t)}{\partial t^2} + \nabla\Big(\nabla \cdot \vec{E}(\vec{r}, t)\Big). \tag{2.15}$$

In the temporal Fourier domain equation (2.15) can be written as

$$\nabla^2\vec{\hat{E}}(\vec{r})+\frac{\omega^2}{c_{E,0}^2}\vec{\hat{E}}(\vec{r})=-\vec{\hat{S}}_E^{pr}(\vec{r})-\omega^2\chi_E(\vec{r})\vec{\hat{E}}(\vec{r})+\nabla\left(\nabla\cdot\vec{\hat{E}}(\vec{r})\right), \tag{2.16}$$

where $\vec{\hat{S}}_E^{pr}(\vec{r})$ is the primary source term of the electric field given as $\vec{\hat{S}}_E^{pr}(\vec{r}) = -i\omega\mu_0\vec{\hat{J}}^{pr}(\vec{r})$, $\chi_E(\vec{r})$ the contrast for the electric field given by

$$\chi_E(\vec{r})=\frac{1}{c_E^2(\vec{r})}-\frac{1}{c_{E,0}^2}, \tag{2.17}$$

with $c_E(\vec{r})$ the speed of light at position $\vec{r}$ and $c_{E,0}$ the speed of light within the background medium. These speed of lights are defined by $c_E^{-2}(\vec{r}) = \mu_0\epsilon(\vec{r})$ and $c_{E,0}^{-2} = \mu_0\epsilon_0$. The second term in equation (2.16) can also be regarded as the electromagnetic contrast source, $\vec{\hat{w}}_E(\vec{r}) = \chi_E(\vec{r})\vec{\hat{E}}(\vec{r})$.

Similar as for acoustic waves, the electric wave field can be described by an integral equation of the second kind,

$$\vec{\hat{E}}(\vec{r})=\vec{\hat{E}}^{inc}(\vec{r})+\vec{\hat{E}}^{sct}(\vec{r}), \tag{2.18}$$

where the incident electric field $\vec{\hat{E}}^{inc}(\vec{r})$ and the scattered electric field $\vec{\hat{E}}^{sct}(\vec{r})$ are given by

$$\vec{\hat{E}}^{inc}(\vec{r})=\int_{\vec{r}'\in\mathbb{S}}\hat{G}_E(\vec{r}-\vec{r}')\vec{\hat{S}}_E^{pr}(\vec{r}')dV(\vec{r}') \tag{2.19}$$

and

$$\vec{\hat{E}}^{sct}(\vec{r})=\omega^2\int_{\vec{r}'\in\mathbb{D}}\hat{G}_E(\vec{r}-\vec{r}')\vec{\hat{w}}_E(\vec{r}')dV(\vec{r}')=\omega^2\int_{\vec{r}'\in\mathbb{D}}\hat{G}_E(\vec{r}-\vec{r}')\chi_E(\vec{r}')\vec{\hat{E}}(\vec{r}')dV(\vec{r}'), \tag{2.20}$$

where $\hat{G}_E(\vec{r}-\vec{r}')$ is the Green's function for the electric field. Because the electromagnetic wave fields are vectorial quantities, a distinction is made between incident transverse electric (TE) waves and transverse magnetic (TM) waves. The Green's function for the electric field for the 2-D case using TE and TM waves and for the 3-D case, are given by [49]

$$\hat{G}_E^{2D,TE}(\vec{r}-\vec{r}')=\left(1+\frac{c_{E,0}^2}{\omega^2}\nabla\nabla\cdot\right)\frac{-i}{4}H_0^{(1)}(\omega|\vec{r}-\vec{r}'|/c_{E,0}), \tag{2.21}$$

$$\hat{G}_E^{2D,TM}(\vec{r}-\vec{r}')=\frac{-i}{4}H_0^{(2)}(\omega|\vec{r}-\vec{r}'|/c_{E,0}), \tag{2.22}$$

$$\hat{G}_E^{3D}(\vec{r}-\vec{r}')=\left(1+\frac{c_{E,0}^2}{\omega^2}\nabla\nabla\cdot\right)\frac{e^{-i\omega|\vec{r}-\vec{r}'|/c_{E,0}}}{4\pi|\vec{r}-\vec{r}'|}. \tag{2.23}$$

A derivation of these functions is given in Appendix A, [45, 50, 51].

2.2. Separate solution methods

The inverse or imaging problem is the problem where the wave field incident in the embedding and the measured wave field recorded by the receivers on the surface $\mathbb{S}$ are known, but where the contrast and the total field within domain $\mathbb{D}$ are unknown. In the following subsections solution methods to solve this highly underdetermined problem are discussed.

2.2.1. Born inversion

One method to solve the inverse imaging problem is called Born inversion (BI) or linear inversion. Here the problem is linearized by replacing the total field in the integral equation with the incident field. This is called the Born approximation, and reduces the equations for the scattered acoustic field (2.8) to

$$\hat{p}^{sct}(\vec{r}) = \omega^2 \int_{\vec{r}' \in \mathbb{D}} \hat{G}_A(\vec{r} - \vec{r}')\chi_A(\vec{r}')\hat{p}^{inc}(\vec{r}')dV(\vec{r}'), \tag{2.24}$$

and the scattered electric field (2.20) to

$$\vec{\hat{E}}^{sct}(\vec{r}) = \int_{\vec{r}' \in \mathbb{D}} \hat{G}_E(\vec{r} - \vec{r}')\chi_E(\vec{r})\vec{\hat{E}}^{inc}(\vec{r}')dV(\vec{r}'). \tag{2.25}$$

This simplification of the problem however results in artifacts that arise due to neglected multiple scattering effects and incorrectly included phase shifts, both caused by spatial variations in speed of sound or speed of light within the media.

The contrast is iteratively estimated using the conjugate gradient scheme on minimizing the L2-norm in the error, which generally reads for both fields:

$$Err^{(n)} = \frac{||\hat{f}^{meas} - \hat{G} * (\omega^2 \hat{f}^{inc}\chi^{(n)})||_{\mathbb{S}}^2}{||\hat{f}^{meas}||_{\mathbb{S}}^2}, \tag{2.26}$$

with $Err^{(n)}$ the normalized error in the data equation, $\chi^{(n)}$ the contrast, $\hat{G}$ the Green's function, $*$ the spatial convolution operator, $\hat{f}^{inc}$ and $\hat{f}^{meas}$ incident and the measured scattered field, all for either the acoustic or electromagnetic field at the n-th iteration, and the subscript $\mathbb{S}$ denotes the inner product over ω and the receiver locations $\vec{r}^{rec} \in \mathbb{S}$ for each source.

The conjugate gradient scheme has the following general form:

$$\begin{aligned} d^{(n)} &= \mathrm{L}^{\dagger} r^{(n-1)}, \\ \alpha^{(n)} &= \frac{\mathrm{Re} < r^{(n-1)}, \mathrm{L}\, d^{(n)} >}{||\mathrm{L}\, d^{(n)}||^2}, \\ \chi^{(n)} &= \chi^{(n-1)} + \alpha^{(n)} d^{(n)}, \\ r^{(n)} &= \hat{f}^{meas} - \mathrm{L}\, \chi^{(n)}, \end{aligned}$$

where $d^{(n)}$ and $\alpha^{(n)}$ are the update direction and amplitude at the n-th iteration, $r^{(n)}$ is the residual at the n-th iteration and L is the general operator given by $\mathrm{L}\chi^{(n)} = \hat{G} * (\omega^2 \hat{f}^{inc}\chi^{(n)})$, where $*$ denotes a spatial convolution and $\hat{G}$ is the general Green's function.

2.2.2. Contrast source inversion

A solution method that does account for multiple scattering is contrast source inversion (CSI) or full-waveform inversion, as for example described in [52]. This non-linear inversion method does not operate within the Born approximation. Instead it defines contrast sources for the acoustic and electromagnetic fields, $\hat{w}_A(\vec{r})$ and $\vec{\hat{w}}_E(\vec{r})$, respectively, hence

$$\hat{w}_A(\vec{r}) = \hat{p}(\vec{r})\chi_A(\vec{r}), \tag{2.27}$$

$$\vec{\hat{w}}_E(\vec{r}) = \vec{\hat{E}}(\vec{r})\chi_E(\vec{r}). \tag{2.28}$$

Now, the error to be minimized consists of the normalized error in the data equation, $Err_S^{(n)}$, as well as the normalized error in the object equation, $Err_D^{(n)}$, given by

$$Err_S^{(n)} = \frac{||\hat{f}^{meas} - \hat{G} * \left(\omega^2 \hat{w}^{(n)}\right)||_{\mathbb{S}}^2}{||\hat{f}^{meas}||_{\mathbb{S}}^2}, \tag{2.29}$$

$$Err_D^{(n)} = \frac{||\hat{w}^{(n)} - \chi^{(n)}\left(\hat{f}^{inc} + \hat{G} * \left(\omega^2 \hat{w}^{(n)}\right)\right)||_{\mathbb{D}}^2}{||\chi^{(n)}\hat{f}^{inc}||_{\mathbb{D}}^2}, \tag{2.30}$$

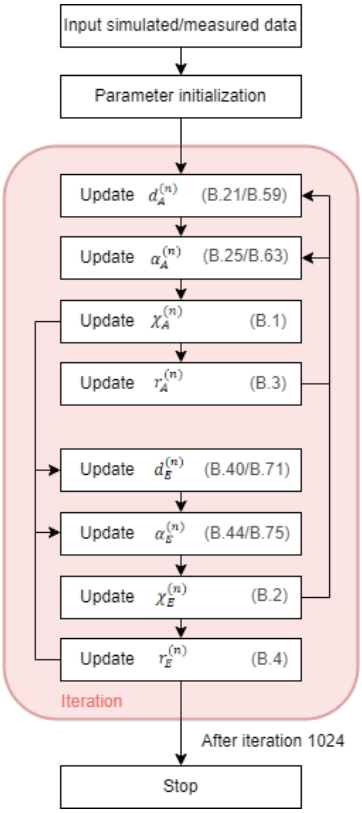

Figure 2.1: General flowchart of the joint inversion algorithm, including references to equations of parameters in case of the CG-/GD method.

where $\hat{w}^{(n)}$ is the contrast source at the n-th iteration, $\hat{f}^{(n)}$ is the total field at the n-th iteration and $\hat{f}^{meas}$ is the measured scattered field, all for either the acoustic or the electromagnetic case and the subscript $\mathbb{D}$ denotes the inner product over ω and all discretized locations $r \in \mathbb{D}$ for each source. When the contrast source is determined, the total fields can be obtained via equations (2.6) and (2.8) for the acoustic field and (2.18) and (2.20) for the electric field.The total additive error function to be minimized is written as

$$Err^{(n)} = Err_S^{(n)} + Err_D^{(n)}. \tag{2.31}$$

The conjugate gradient scheme for the contrast source inversion, including the Polak-Ribière coefficient, $\gamma^{(n)}$, in the general form is written as,

$$g^{(n)} = \frac{\mathrm{L}_{\mathbb{S}}^{\dagger} r_s^{(n-1)}}{||\hat{f}^{meas}||_{\mathbb{S}}^2} + \frac{r_d^{(n-1)} - \chi^{(n-1)} \mathrm{L}_{\mathbb{D}}^{\dagger} r_d^{(n-1)}}{||\chi^{(n-1)} \hat{f}^{inc}||_{\mathbb{D}}^2},$$

$$\gamma^{(n)} = \frac{|< g^{(n)}, g^{(n)} - g^{(n-1)} >_{\mathbb{D}}|}{||g^{(n-1)}||_{\mathbb{D}}^2},$$

$$d^{(n)} = g^{(n)} + \gamma^{(n)} d^{(n-1)},$$

$$\alpha^{(n)} = \frac{\mathrm{Re} < g^{(n)}, d^{(n)} >_{\mathbb{D}}}{||\mathrm{L}_{\mathbb{S}}\, d^{(n)}||_{\mathbb{S}}^2 / ||\hat{f}^{meas}||_{\mathbb{S}}^2 + ||\chi^{(n-1)} \mathrm{L}_{\mathbb{D}}\, d^{(n)}||_{\mathbb{D}}^2 / ||\chi^{(n-1)} \hat{f}^{inc}||_{\mathbb{D}}^2},$$

$$\hat{w}^{(n)} = \hat{w}^{(n-1)} + \alpha^{(n)} d^{(n)},$$

$$\hat{f}^{(n)} = \hat{f}^{inc} + \mathrm{L}_{\mathbb{D}}\, \hat{w}^{(n)},$$

$$\chi^{(n)} = \frac{\mathrm{Re} < \hat{f}^{(n)}, \hat{w}^{(n)} >_{\mathbb{S}}}{||\hat{f}^{(n)}||_{\mathbb{S}}^2},$$

$$r_s^{(n)} = \hat{f}^{meas} - \mathrm{L}_{\mathbb{S}}\, \hat{w}^{(n)},$$

$$r_d^{(n)} = \chi^{(n)} \hat{f}^{inc} + \chi^{(n)} \mathrm{L}_{\mathbb{D}}\, \hat{w}^{(n)} - \hat{w}^{(n)},$$

where $g^{(n)}$ is the steepest direction, $\hat{f}^{(n)}$ the total field, $r_s^{(n)}$ the state residual, and $r_d^{(n)}$ the data residual, all for either the acoustic or the electric case at the n-th iteration and $\mathrm{L}_{\mathbb{S}}$ is the data operator given by $\mathrm{L}_{\mathbb{S}}\, x = \hat{G} *_{\mathbb{S}} (\omega^2 x)$ and $\mathrm{L}_{\mathbb{S}}$ is the object operator given by $\mathrm{L}_{\mathbb{D}}\, x = \hat{G} *_{\mathbb{D}} (\omega^2 x)$.

2.3. Joint solution methods

A possible method to overcome problems associated with separate inversion like low resolution or difficulties in distinguishing materials or tissues, is joint inversion based on structural constraints. The main idea is to let the acoustic and electromagnetic inversion constrain each other, by assuming that the material boundaries, and therefore the parameter boundaries are at the same locations. The general flowchart of a joint inversion algorithm, based on separate BI, is shown in Figure 2.1.

To create such a joint inversion algorithm, an extra error to be minimized must be incorparated in the error function for BI (2.26) and for CSI (2.31). Having boundaries at the same locations, means that the level sets of both parameter profiles should be parallel. Consequently, the normals to these levels sets, which are the gradients of the parameter profiles, must also be parallel. Additionally it is desired that the error included, converges to zero when the structural constraint is met.

Two types of constraints that meet these criteria, are the cross-gradient (CG) and the gradient difference (GD) constraints. Both constraints update in an alternative matter, using back propagation as a starting point. Within each iteration, the acoustic contrast is updated first, followed by the electromagnetic contrast, as shown in Figure 2.1. The reason for starting with the acoustic inversion is that the initial acoustic resolution is assumed to be better than the electromagnetic resolution. The two types of constraints are further discussed in the next paragraphs.

2.3.1. Cross-gradient constraint

The first constraint that can serve as a structural constraint is the cross-product of the gradients of the contrasts, which in short is called the cross-gradient (CG), first proposed by [28]. The cross-product of two parallel identities goes to zero, and therefore both conditions described above are met. The normalized form of the CG constraint at the n-th iteration, $Err_{A,CG}^{(n)}$, for the acoustic case and $Err_{E,CG}^{(n)}$, for the electromagnetic case, are given by

$$Err_{A,CG}^{(n)} = \frac{||\nabla\chi_A^{(n)} \times \nabla\chi_E^{(n-1)}||^2}{||\nabla\chi_A^{(n-1)} \times \nabla\chi_E^{(n-1)}||^2}, \tag{2.32}$$

$$Err_{E,CG}^{(n)} = \frac{||\nabla\chi_A^{(n)} \times \nabla\chi_E^{(n)}||^2}{||\nabla\chi_A^{(n-1)} \times \nabla\chi_E^{(n-1)}||^2}. \tag{2.33}$$

The difference in the iteration of the contrasts between the numerators of equations (2.32) and (2.33) is due to the acoustic contrast being updated first within each iteration. The update direction and amplitude in the conjugate gradient scheme, have been derived for the additive form of the error functions for both the acoustic and electromagnetic field as shown in Appendix B.1

2.3.2. Gradient difference constraint

Another method proposed by [41], is the gradient difference (GD) approach. Here the difference in gradients of the contrasts is used as a constraint, the normalized form of the GD constraint at the n-th iteration, $Err_{A,GD}^{(n)}$, for the acoustic case, and $Err_{E,GD}^{(n)}$, for the electromagnetic case are given by

$$Err_{A,GD}^{(n)} = ||\nabla\overline{\chi}_A^{(n)} - \nabla\overline{\chi}_E^{(n-1)}||^2, \tag{2.34}$$

$$Err_{E,GD}^{(n)} = ||\nabla\overline{\chi}_A^{(n)} - \nabla\overline{\chi}_E^{(n)}||^2, \tag{2.35}$$

where $\overline{\chi}_A^{(n)}$ and $\overline{\chi}_E^{(n)}$ are acoustic and electromagnetic contrast, normalized by the maximum of the absolute real value. Note that the acoustic contrast is updated first within the same iteration, resulting in a difference in iterations of the normalized contrasts in equations (2.34) and (2.35). The derivation of the corresponding update direction and amplitude in the conjugate gradient scheme, is shown in Appendix B.2, for both the acoustic and the electromagnetic case.

3

Methods

In this chapter the methodology to test the proposed methods is discussed. First a general overview of the study is given, next the details of the forward and inverse simulations are provided.

As this project serves as a first framework for further research in the field of joint inversion, the verification of the joint inversion algorithm is completely based on synthetic results. Forward simulation and inversion are executed for both acoustic and electromagnetic fields, using a synthetic model. Next, two joint inversion algorithms are tested and compared to the separate inversion data. The details of the inversions algorithms are discussed in the previous chapter. For all simulations, FORTRAN 90 is used as the programming language. MATLAB R2020a is used for the subsequent image visualisation.

3.1. Forward problem

The forward wave field propagation and scattering is simulated using the existing code for the acoustic case by K.W.A. van Dongen, as used in [53], which was extended to the electromagnetic case. Two numerical models are used as input in the simulations. The speed of sound and speed of light profiles of model 1 have gradients pointing in the same direction and are shown in Figures 3.1(e) and 3.1(g) respectively. In model 2 the gradients speed of sound and speed of light point in opposite directions, of which the profiles are depicted in 3.1(f) and 3.1(h). The background speed of sound for both models is 1500 $\mathrm{m/s}$ and the background speed of light is 2.25 $\cdot 10^8$ $\mathrm{m/s}$, corresponding to a relative permittivity, ε_r, of 1.78. The parameter settings of the other components of the model are shown in Table 3.1. The model is discretized in 64x64 pixels, with a pixel length, Δx, of 1.5 mm.

In the forward simulations, 16 sources and 128 receivers are used, positioned in a ring around the contrast. The source positions are indicated by a black asterisk in figure 3.1(e-h). Each source is excited with a center frequency of $f_{A,0}$ = 0.1 MHz in the acoustic case and $f_{E,0}$ = 1 GHz in the electromagnetic case. The source pulses are shown in the time and frequency domain in figure 3.1(a) and 3.1(c) for the acoustic case and in 3.1(b) and 3.1(d) for the electromagnetic case. The timestep, Δt, is set to 1/15-th of the center frequency, giving Δt_A = 6.67$\cdot 10^{-7}$ s and Δt_E = 6.67$\cdot 10^{-11}$ s. The number of time steps, N_t, is set for the acoustic case to $N_{t,A}$ = 540 and the electromagnetic case to $N_{t,E}$ = 72.

Table 3.1: Speed of sound, c_A in $\mathrm{m/s}$, speed of light, c_E in $\mathrm{m/s}$ and relative permittivity, ε_r, of different components in the models.

	Model 1			Model 2		
	c_A (m/s)	c_E (m/s)	ε_r (-)	c_A (m/s)	c_E (m/s)	ε_r (-)
Background	1500	2.250 $\cdot 10^8$	1.780	1500	2.250 $\cdot 10^8$	1.780
T	1550	2.300 $\cdot 10^8$	1.700	1550	2.200 $\cdot 10^8$	1.860
U	1450	2.200 $\cdot 10^8$	1.860	1450	2.300 $\cdot 10^8$	1.700
Circle	1525	2.275 $\cdot 10^8$	1.740	1525	2.225 $\cdot 10^8$	1.820

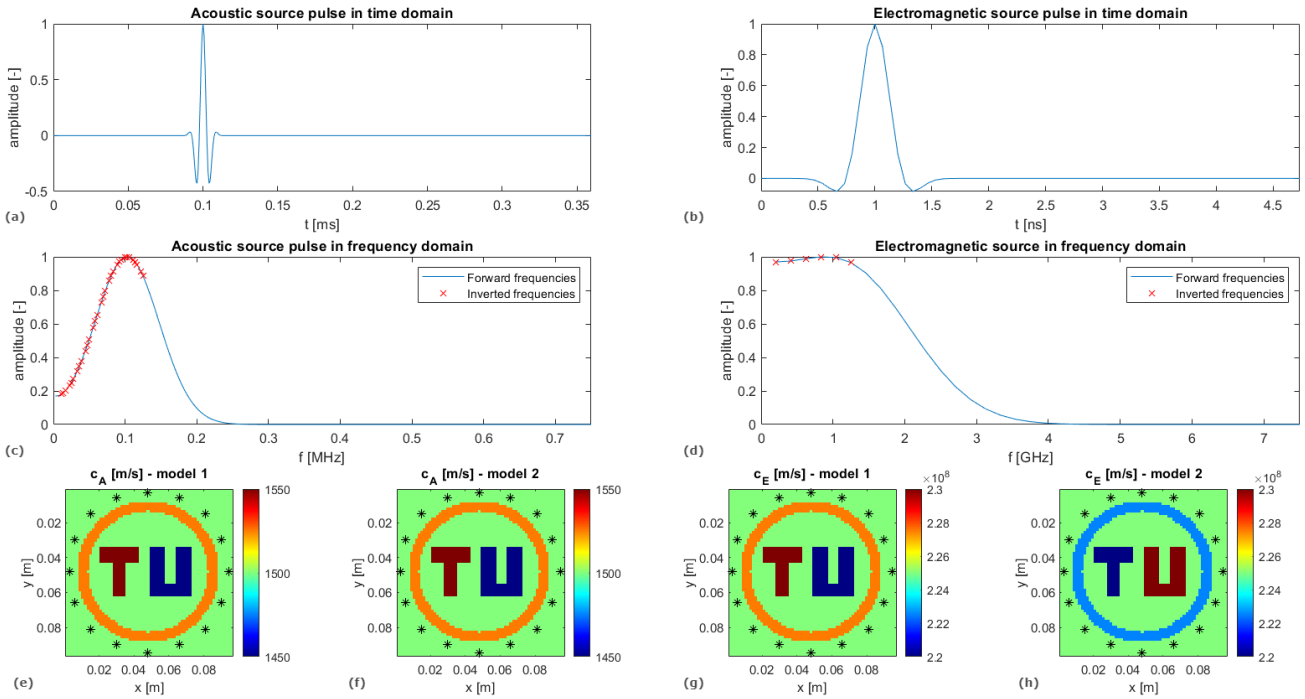

Figure 3.1: Overview of modeled input. Acoustic case: source pulse in time domain (a) and frequency domain (c), speed of sound profiles of model 1 (e) and model 2 (f). Electromagnetic case: source pulse in time domain (b) and frequency domain (d), speed of light profiles of model 1 (g) and model 2 (f). In (c) and (d) the selected frequencies for inversion are indicated with a red x. In (e)-(h) the source locations are indicated with a black asterisk.

3.2. Inverse problem

To compare the conventional separate inversion to the proposed joint inversion methods based on structural constraints, both reconstruction methods are applied to the data obtained by solving the forward problem for all cases and models. The comparison is done by qualitative comparison, as well as a numerical comparison using the mean square error (MSE), given by

$$MSE = \frac{||\chi^{true} - \chi^{inv}||^2}{||\chi^{true}||^2}, \tag{3.1}$$

where χ^{true} are the contrast values of the model and χ^{inv} are the values of the inverted contrast.

The existing code as used in [53], is used as the separate inversion algorithms for the acoustic case and is extended to the electromagnetic case, for both BI and CSI.

Two types of constraints are added to the separate BI algorithms. Both the CG constraint and the GD constraint, of which the details are described in Section 2.3, are implemented and tested. In a first verification, the two synthetic models of the acoustic parameters are used as the input for the electromagnetic joint inversion. Subsequently, simultaneous inversion is tested for both types of constraints, for both models. The extension to a joint CSI algorithm has not yet been realized in this project.

To speed up the inversion processes, a limited number of frequencies is used in both the separate and joint inversion, which are indicated with a red x in figures 3.1(c) and 3.1(d). The frequencies are selected out of the range of 0.1 to 1.25 times the center frequency of the Gaussian pulse. Less frequencies are selected in the electromagnetic case, due to a relatively higher frequency interval, which is in turn restricted due to the time step size and speed of light of the background medium. All inversion algorithms run for 1024 iterations.

Some modifications to the algorithms described in Chapter 2 are implemented. In case of the joint inversion with the GD constraint, the contrasts, $\chi_A^{(n)}$ and $\chi_E^{(n)}$, and the update directions, $d_A^{(n)}$ and $d_E^{(n)}$, were set to zero at the source and receiver locations and one pixel adjacent to it in each direction at each iteration, to avoid artifacts in the reconstructions at these locations. Next, at each iteration, the values of the reconstructed contrasts that exceed the maximum value of the synthetic contrast used as the input, are set to that maximum value. Similarly, the values of the reconstructed contrasts that are lower than the minimum value of the synthetic contrast values, are set to that minimum value.

Finally, in both of the joint inversion algorithms, a ratio $\psi^{(n)}$ has been added in the total update directions as described in equations (B.21, B.40) for the CG constraint, and (B.59, B.71) for the GD constraint, both for the acoustic and electromagnetic case, respectively. The update directions in case of the CG constraint equal

$$d_A^{(n)} = d_{A,BI}^{(n)} + \psi_{A,CG}^{(n)} d_{A,CG}^{(n)} = L_A^{\dagger} r_A^{(n-1)} + \psi_{A,CG}^{(n)} \nabla \cdot \left[\nabla \chi_E^{(n-1)*} \times \left(\nabla \chi_A^{(n-1)} \times \nabla \chi_E^{(n-1)} \right) \right], \tag{3.2}$$

$$d_E^{(n)} = d_{E,BI}^{(n)} + \psi_{E,CG}^{(n)} d_{E,CG}^{(n)} = L_E^{\dagger} r_E^{(n-1)} + \psi_{E,CG}^{(n)} \nabla \cdot \left[\nabla \chi_A^{(n)*} \times \left(\nabla \chi_E^{(n-1)} \times \nabla \chi_A^{(n)} \right) \right], \tag{3.3}$$

with the ratio of the update directions of the CG constraint $\psi_{A,CG}^{(n)}$ and $\psi_{E,CG}^{(n)}$ at the n-th iteration being

$$\psi_{A,CG}^{(n)} = \frac{d_{A,BI,Max}^{(n)}}{d_{A,CG,Max}^{(n)}}, \tag{3.4}$$

$$\psi_{E,CG}^{(n)} = \frac{d_{E,BI,Max}^{(n)}}{d_{E,CG,Max}^{(n)}}, \tag{3.5}$$

where the subscript Max indicates the maximum value of the real part. The update directions in case of the GD constraint are now written as

$$d_A^{(n)} = d_{A,BI}^{(n)} + \psi_{A,GD}^{(n)} d_{A,GD}^{(n)} = L_A^{\dagger} r_A^{(n-1)} + \psi_{A,GD}^{(n)} \nabla^2 \left(\overline{\chi}_A^{(n-1)} - \overline{\chi}_E^{(n-1)} \right)^*, \tag{3.6}$$

$$d_E^{(n)} = d_{E,BI}^{(n)} + \psi_{E,GD}^{(n)} d_{E,GD}^{(n)} = L_E^{\dagger} r_E^{(n-1)} + \psi_{E,GD}^{(n)} \nabla^2 \left(\overline{\chi}_E^{(n-1)} - \overline{\chi}_A^{(n)} \right)^*, \tag{3.7}$$

with the ratio of the update directions of the GD constraint, $\psi_{A,GD}^{(n)}$ and $\psi_{E,GD}^{(n)}$, given as

$$\psi_{A,GD}^{(n)} = \frac{d_{A,BI,Max}^{(n)}}{d_{A,GD,Max}^{(n)}}, \tag{3.8}$$

$$\psi_{E,GD}^{(n)} = \frac{d_{E,BI,Max}^{(n)}}{d_{E,GD,Max}^{(n)}}. \tag{3.9}$$

4

Results

This chapter gives an overview of the results obtained by the methods described in the previous chapter. First, results of the forward simulation are shown, next a comparison between separate inversion and joint inversion with the CG constraint is given and lastly, the results of the separate inversion and the joint inversion with the GD constraint are compared.

4.1. Forward simulations

The wave propagation of the pressure wave field and the electric wave field through both of the models are shown in Figure 4.1, which are screenshots of the scattered and total wave fields. It is clearly visible that the electromagnetic wavelength is significantly larger than the acoustic wavelength; the center wavelengths are $\lambda_{A,0}$ = 15 mm for the acoustic case and $\lambda_{E,0}$ = 225 mm for the electromagnetic case. On top of that, as the acoustic profiles of the two models are the same, the pressure fields are also equal. The electric fields differ only slightly between the two models, as the shape of the models and the norm of the gradients are equal; the gradients only differ in sign.

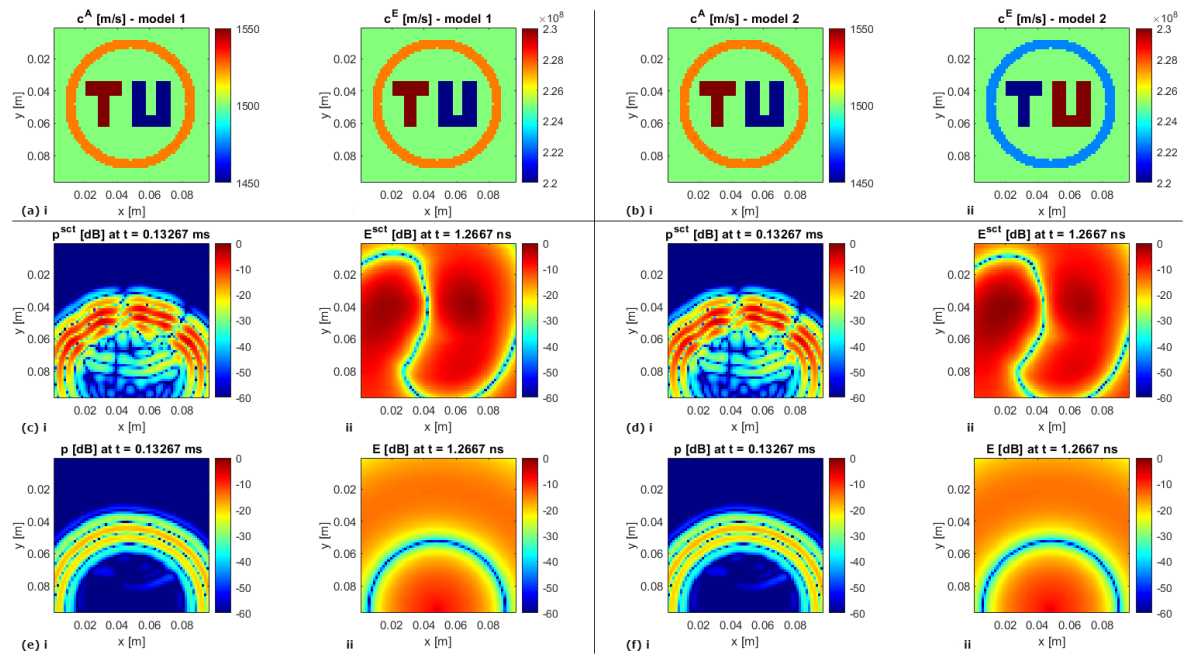

Figure 4.1: Models, screenshots of pressure fields at t_A = 0.133 ms and screenshots of electric fields at t_E = 1.27 ns. Speed profiles (a) & (b), scattered fields (e) & (d) and total fields (f) & (g), of model 1 and 2 respectively. The subfigures indicated with *i* are for the acoustic case: speed of sound and pressure fields, and the subfigures indicated with *ii* are for the electromagnetic case: speed of light and electric fields.

Table 4.1: MSE's of separate, joint with CG constraint and joint with GD constraint inversion results, for model 1 and model 2.

		Model 1		Model 2	
		MSE_A	MSE_E	MSE_A	MSE_E
Separate	BI	0.115	0.507	0.115	**0.523**
	CSI	**0.071**	0.596	**0.071**	0.601
Joint - CG	syn in	-	0.674	-	0.865
	no syn in	0.513	0.917	0.620	0.899
Joint - GD	syn in	-	**0.284**	-	1.45
	no syn in	0.089	0.460	0.261	0.951

4.2. Inversion results

The inversion results are summarized in Figure 4.2. The corresponding MSE's are shown in Table 4.1. The separate and joint results of the different constraints are discussed subsequently.

Separate inversion

The separate BI results are shown in Figures 4.2(c) and 4.2(d), for model 1 and 2 respectively. In the acoustic results expected multiple scattering artefacts due to the Born approximation are visible, but a good resolution and MSE_A of 0.115 is obtained. The reconstructed speed of light profiles show very low resolution due to the large wavelength. Consequently, the MSE_E for model 1 and 2, being 0.507 and 0.523, are significantly larger compared to the acoustic case. The results of CSI, 4.2(e) and 4.2(f) for model 1 and 2 respectively, show improved results in the acoustic case with an MSE_A of 0.071, as multiple scattering effects are no longer neglected. The electromagnetic profiles do not improve compared to BI, as the resolution of the data is too low to benefit from the more advanced inversion algorithm. The MSE_E's for CSI of model 1 and 2 are 0.596 and 0.601.

Joint inversion - cross-gradient

The speed profiles resulting from the joint inversion with the CG constraint, using the acoustic synthetic model as an input for the electromagnetic inversion, are shown in Figures 4.2(g)i and 4.2(h)i, for model 1 and 2. No MSE_A is assigned, since the output is the true model for the speed of sound. In the electromagnetic case, we see a clear profile of the edges of the characters in the speed of light profile of both models. However the speed of light distribution is not following these boundaries, leading to MSE_E's of 0.674 and 0.865 for model 1 and 2 respectively. The color bar in 4.2(h)ii also indicates that when using model 2, the inversion has trouble reconstructing the full range of speed of light values, compared to separate inversion, causing the high MSE_E in case of model 2.

When inverting both data sets retrieved by the forward simulations, we see the joint inversion destroys the structure of the acoustic speed of sound profile, as shown in Figures 4.2(i)i and 4.2(j)i, with a corresponding MSE_A of 0.513 and 0.620. On top of that, the electromagnetic results, Figures 4.2(i)ii and 4.2(j)ii, do not benefit from the joint inversion and the characters cannot be recognized, yielding an MSE_E of 0.917 for model 1 and 0.620 for model 2.

Joint inversion - gradient difference

The reconstructed speed profiles by joint inversion with the GD constraint, show promising results when using model 1. Both when using the synthetic acoustic model as input for the electromagnetic inversion, Figure 4.2(k), and when inverting the both the data sets in alternating fashion, Figure 4.2(m), the electromagnetic results show a clear structure of the characters in the imaged model. Not only the edges are visible, but also the inner structure is inverted more correctly, yielding improved MSE_E's of 0.284 and 0.460, for the synthetic acoustic input and the simulated acoustic input respectively. The acoustic image, Figure 4.2(m)i, is qualitatively comparable to the separate inversions and has a slightly improved MSE_A of 0.089 compared to the separate BI.

Nevertheless, when using model 2 with the acoustic and electromagnetic contrast gradients with opposite sign, the inversion fails. In the case of using the synthetic model, Figure 4.2(l), we see an imprint of the characters TU in the speed of light profile, but the values within the contrasts are inverted in

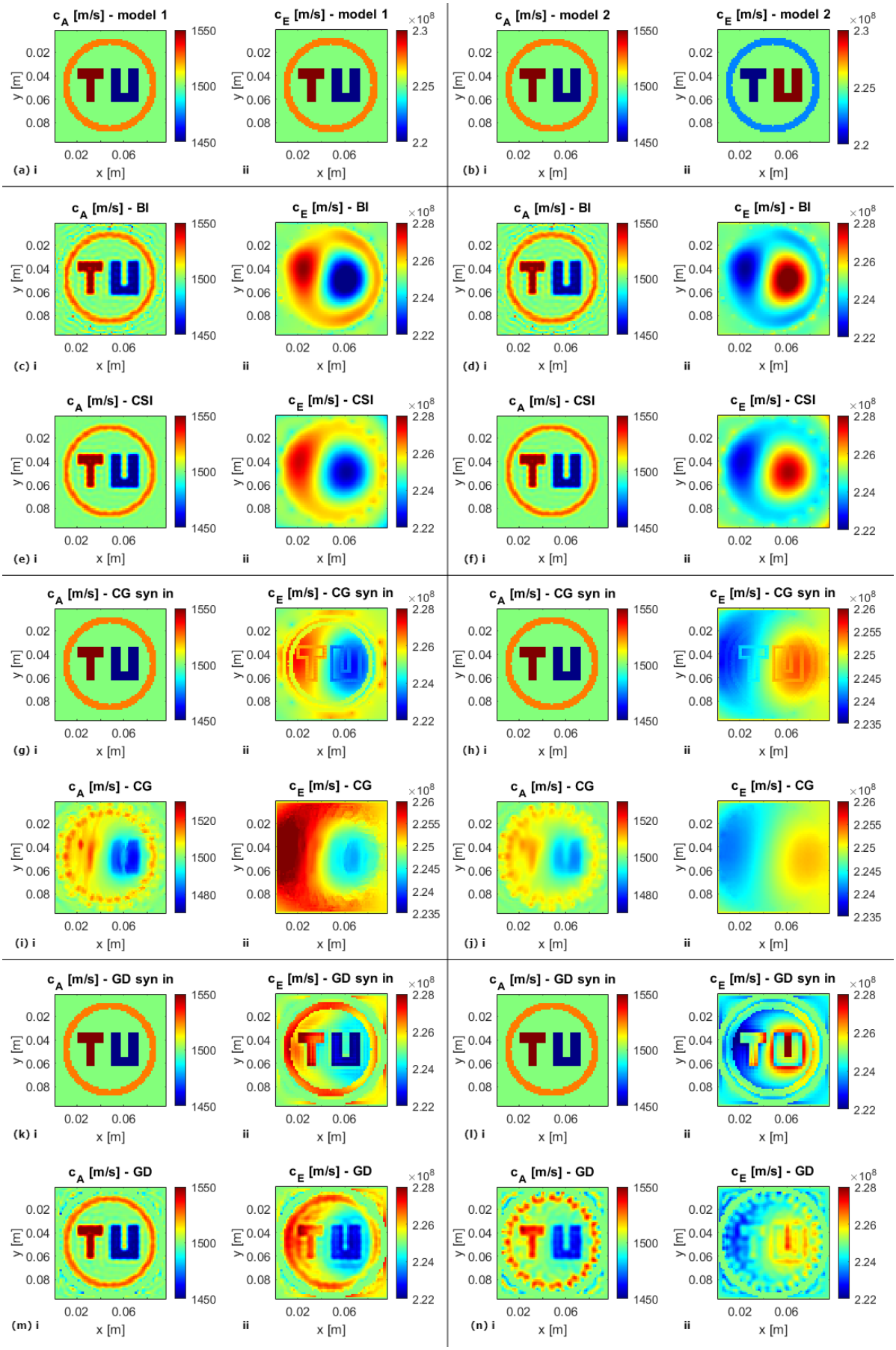

Figure 4.2: Profiles of tested models 1 (a) & 2 (b). Inversion results of separate BI (c) & (d) and CSI (e) & (f), joint with CG constraint using acoustic synthetic input (g) & (h) and alternating inversion (i) & (j), joint with GD constraint using acoustic synthetic input (k) & (l) and alternating inversion (m) & (n), for 1 & 2 respectively. All subfigures indicated with *i* are acoustic results and with *ii* are electromagnetic results. Note that to enhance readability colorbars vary among the subfigures.

the wrong direction, resulting in an MSE_E of 1.45. When using both the data sets, Figure 4.2(n), some structure can still be seen in the electromagnetic case, however the range on inverted values is less accurate compared to the separate inversion when comparing the color bars, which gives the poor MSE_E of 0.951. Also the acoustic result now shows less structure compared to separate inversion, and has an MSE_A of 0.261.

Finally, in the overview of the MSE's of all types of inversions given in Table 4.1, the bold values are the most accurate values of the type of wave of all types of inversions. We see that only for the GD constraint in the electromagnetic case of model 1, the joint inversion has an improved MSE over the separate inversions, most significantly visible when using the synthetic acoustic model as input for the electromagnetic inversion. Nevertheless, the joint inversion with GD constraint inverting both data sets, gives a slightly improved MSE for both the acoustic and the electromagnetic case compared to BI. The qualitatively improvement in the electromagnetic inversion results is more impressive than the MSE, as the structure of the contrast is now revealed, where it is completely absent in the separate inversion. The values in the edges, outside the circle of the source and receiver locations, is off in the joint GD electromagnetic case, and probably affects the MSE, while being less important for recognizing structure.

5 Discussion

In this chapter, some final remarks and points of discussions are presented. First, a discussion on the different implemented constraints, CG and GD, are given, including recommendations for further research. Next, a view on the translation of the presented research to future applications are given, especially focusing on the choice of parameters and reflecting on the type of joint inversion most viable for applications.

5.1. Implemented constraints

The shortcomings and corresponding possible explanations of both the presented constraints are discussed in this section, as well as recommendations on how to overcome these shortcomings.

5.1.1. Cross-gradient constraint

From the results it is clear that the reconstructions when using the CG constraint are not satisfactory. However, the use of the acoustic model as input for the electromagnetic joint CG inversion, has shown that the algorithm is capable of detecting structures in the electromagnetic contrast profile that were otherwise hidden. To avoid the error function to only work on the boundaries of the different materials, one should assure that the error function does not go to zero within the different materials. In other words, for both modalities, the gradient should not equal zero for the CG error function to do anything at that point. A way to avoid the error function from going to zero at homogeneous regions within the inverted data, could be by adding some noise or speckle to the acoustic starting model before using it as input for the electromagnetic inversion.

On top of that, when using the simulated acoustic data as input for the joint CG inversion, the behaviour of reconstructing the outline of the contrast is no longer expected. When inverting the acoustic data, the gradients are usually not absolutely zero, which becomes apparent from the resulting reconstructions. Here, the outline of the boundary is no longer visible. Unfortunately, these results do not only show no improvement in the electromagnetic reconstruction, but also destroy the structure in the acoustic reconstruction. A possible explanation for these disappointing results is that the resolution of the electromagnetic reconstruction dominates the joint inversion process. It can be interesting to redo the simulations using a higher center frequency for the electromagnetic wave fields of for example 8 GHz, so some initial structure is visible after the first iteration of the electromagnetic data.

5.1.2. Gradient difference constraint

The reconstructions using the GD constraint of model 1 are remarkable, especially when considering the low resolution of the separate electromagnetic reconstruction. Nevertheless, the algorithm fails when using a model with the gradients of the speed of sound profile opposite to the gradients of the speed of light profile. Effectively, this means the gradient difference model so far cannot be used for any realistic sample to be imaged. It is therefore necessary to investigate how the GD constraint can be extended such that opposite gradients do not form a problem.

One possible solution for the problem of constructing the wrong update direction in case of gradients with different directions between the modalities, might be using the absolute GD of the contrasts. Nonetheless, the absolute value is difficult to minimize, which is necessary in order to find the update parameters. An alternative to the absolute value could be using the square of the GD in stead of the absolute value. However, introducing a square in the L2-norm can cause local minima, causing flaws in the update parameters. Finally, one can adjust the normalization to overcome the sign problem. A proposed way is normalizing the gradient of the contrast, in stead of taking the gradient of the normalized contrast. Note that the normalization should be using the maximum of the absolute value of the gradient of the contrast in a near surrounding, but keeping the sign.

Apart from opposite gradient directions between the two different modalities, different gradient amplitudes have not yet been tested. It would be interesting to see what happens when there is for example only a slight difference in speed of sound between two materials, while there is a large difference in speed of light. It is expected that the GD constraint, will not properly reconstruct these types of models. The normalized difference in gradients will not go to zero for the correct solution of the inversion. However, if the the difference in amplitude between the normalized gradients of the contrasts is small enough, no problems are expected. It is therefore necessary to discover in what range amplitude difference the GD constraint will still be useful, and if the chosen parameters $\psi^{(n)}$ and β can influence the outcome.

Another issue that needs to be solved in future research is the minus sign in the joint part of the acoustic update direction in the GD case. When inspecting the update directions in the simulations it was found this part of the acoustic update direction has the wrong sign. Adding a minus sign in the code solved the problem, leading to the results as presented in Chapter 4. Despite a thorough search for a mistake in the derivation in Appendix B.2.1, as well as in the implementation in the code, no mistakes have been found so far. However, since the idea of the GD method holds conceptually for cases with gradients in the same direction between the acoustic and electromagnetic contrasts, it is most likely there is still an error in the implementation, yet to be found.

A next step to improve the algorithm, is to extend the algorithm to CSI, in contrast to the currently used BI. Especially for cases where strong scatterers are present, and multiple scattering effects play a significant role, CSI can improve the accuracy of the reconstructions. Nevertheless for the model used in this research, no large improvements are expected, since we see no large difference in the separate BI and CSI reconstructions.

Lastly, an interesting approach for the joint inversion constraints, would be to implement a combination of the two algorithms, exploiting the strengths of both constraints. Testing different regularization parameters, a better understanding of both the constraints and their compatibility could be obtained.

5.2. Translation to applications

In order to make the translation from this computational research, to real life applications, both the choice of parameters and the type of joint inversion method are of importance to be considered. In this section both are discussed.

5.2.1. Parameters

In terms of model parameters, it can be fruitful to experiment with several cases to get a better understanding if and how joint inversion can be used for seismic, medical or other applications. First of all, it should be noted that the choice of parameters within this research is rather arbitrary, as it serves as a proof of concept rather than a validation of an implementation. The background speed of sound and speed of light have been chosen to have the values of water. However, the frequency dependence in case of the electromagnetic parameters was not taken into account, causing the speed of light and electric permittivity to not have realistic values for a center frequency of 1 GHz. On top of that, the parameters assigned to the objects embedded in the background are not based on properties of physical materials. For specific applications the acoustic and electromagnetic parameters should be adjusted to realistic combinations, as well as the center frequencies.

In addition to that parameters can be chosen based on real material properties, it is interesting to choose the parameters such that the initial motivational practical limitations of separate inversion are better explored. In this thesis, the focus lies completely on improving the resolution of the electromagnetic inversion results, while the acoustic inversion results can also suffer from indistinguishable materials or tissues. Simulations when using a model with comparable acoustic parameters for different objects, while clearly different electromagnetic parameters, are therefore essential to fully test the applicability of the proposed method in practical situations. Naturally, when all previously described shortcomings are solved and the suggestions are tested, the next step would be to test the joint inversion algorithms using experimental data.

5.2.2. Methods of joint inversion

In this research, we focus on implementing joint inversion using structural information in the most challenging sense: alternatively constraining both data sets by the other. However, we see that with the currently used frequencies, the acoustic reconstructions barely benefit from the joint inversion method. Therefore one can argue, it would be sensible to use the acoustic inversion results as input for the electromagnetic inversion, but not the other way around. The separate inversion could be seen as structural pre-information for the electromagnetic inversion. The advantages over complete joint inversion would be a more accurate structural constraint for the electromagnetic inversion from the first iterations on and a slightly better acoustic inversion result.

6

Conclusions

In this project, two joint Born inversion algorithms based on structural constraints have been developed and tested on two models, first by using the acoustic model as input, followed by using simulated data from both modalities. The most significant improvement in reconstruction resolution, compared to separate inversion, is observed in the electromagnetic joint reconstruction using the gradient difference (GD) approach, on the model with the gradients of the acoustic and electromagnetic parameters pointing in the same direction. The acoustic joint GD reconstruction does not show advantages over separate inversion yet. Nonetheless, the joint inversion based on the GD constraint fails when using a model where the gradients of the acoustic and electromagnetic parameters point in opposite directions.

Additionally, the joint electromagnetic cross-gradient (CG) reconstruction shows some improvements compared to separate inversion by reconstructing an outline of the model, when using the acoustic synthetic model as input for the inversion. However, no improvements are shown here within different structural components. Moreover, when using both simulated data sets as input for the joint CG inversion, the structure in the acoustic results are destroyed, with no improvement in the electromagnetic results to compensate. Nonetheless, the CG approach works equally well on both the model with the gradients pointing in the same direction and the model with gradients pointing in opposite directions for the acoustic and electromagnetic parameters and therefore has a more general working mechanism at this point, compared to the GD approach.

A

Derivation Green's functions

This appendix shows the derivation of the Green's functions for the acoustic and electromagnetic wave fields. The derivation includes both the 2-D and 3-D case.

A.1. Acoustic field

In this work, the Green's function is defined as the impulse response of the homogeneous embedding, or in other words, the field generated by a point source in absence of any contrast. To derive the acoustic or scalar Green's function in the temporal Fourier domain, $\hat{G}_A(\vec{r},\vec{r}')$, the wave equation for a homogeneous medium in the temporal Fourier domain with the source term being a point source needs to be solved, hence

$$\nabla^2\hat{G}_A(\vec{r},\vec{r}') + \frac{\omega^2}{c_{A,0}^2}\hat{G}_A(\vec{r},\vec{r}') = -\delta(\vec{r}-\vec{r}'), \tag{A.1}$$

with position vector, $\vec{r}$, angular frequency ω, the Dirac delta function $\delta(\vec{r}-\vec{r}')$ and the speed of sound of the embedding $c_{A,0}$, defined by $c_{A,0}^{-2} = \rho_0\kappa_0$, with ρ_0 the assumed constant mass density of the medium and κ_0 the compressability of the embedding. Note that from (A.1), the caret symbol, ^, is used to denote quantities in the temporal Fourier domain. The used definition of the Fourier transform is $\hat{G}(\vec{r}) = \int_{-\infty}^{\infty} G(\vec{r},t)e^{i\omega t}dt$. On the infinite domain, and in the special case of $\vec{r}'$ = $\vec{0}$, spherical or circular symmetry arises for the 3-D and 2-D case respectively. First the 3-D case is discussed, followed by the 2-D case.

A.1.1. Three dimensional case

The solution of the 3-D wave equation in (A.1), can be found using an analysis in the real domain [45,46] or in the complex plane [47]. Both derivations are given for completeness.

Real domain derivation

Due to the spherical symmetry in 3-D and considering the case $\vec{r} \neq 0$ and $\vec{r}' = 0$, equation (A.1) reduces to

$$\frac{1}{r^2}\frac{d}{dr}\left[r^2\frac{d\hat{G}_A^{3D}(\vec{r},\vec{0})}{dr}\right] + \frac{\omega^2}{c_{A,0}^2}\hat{G}_A^{3D}(\vec{r},\vec{0}) = 0. \tag{A.2}$$

Multiplying equation (A.2) with r^2, using the product rule on the first term and dividing again by r, yields,

$$2\frac{d\hat{G}_A^{3D}(\vec{r},\vec{0})}{dr} + r\frac{d^2\hat{G}_A^{3D}(\vec{r},\vec{0})}{dr^2} + r\frac{\omega^2}{c_{A,0}^2}\hat{G}_A^{3D}(\vec{r},\vec{0}) = 0. \tag{A.3}$$

Noting the second derivative of $r\hat{G}_A^{3D}(\vec{r},\vec{0})$ can be rewritten as,

$$\frac{d^2}{dr^2}[r\hat{G}_A^{3D}(\vec{r},\vec{0})] = \frac{d\hat{G}_A^{3D}(\vec{r},\vec{0})}{dr} + \frac{d}{dr}\left[r\frac{d\hat{G}_A^{3D}(\vec{r},\vec{0})}{dr}\right] = 2\frac{d\hat{G}_A^{3D}(\vec{r},\vec{0})}{dr} + r\frac{d^2\hat{G}_A^{3D}(\vec{r},\vec{0})}{dr^2}, \tag{A.4}$$

equations (A.3) and (A.4) can be combined into

$$\frac{d^2}{dr^2}\left[r\hat{G}_A^{3D}(\vec{r},\vec{0})\right] + \frac{\omega^2}{c_{A,0}^2} r\hat{G}_A^{3D}(\vec{r},\vec{0}) = 0. \tag{A.5}$$

Equation (A.5) is a second order ordinary differential equation (ODE), which has the solution

$$r\hat{G}_A^{3D}(\vec{r},\vec{0}) = C_1 e^{-i\omega r/c_{A,0}} + C_2 e^{+i\omega r/c_{A,0}}, \tag{A.6}$$

with C_1 and C_2 constants to be determined. The first term in equation (A.6) represents outward propagating waves, while the second term represents inward propagating waves. Since the second term is unphysical, it is disregarded. The remaining solution can be substituted into equation (A.1), integrated over a small sphere centered at $\vec{r}$ = 0 of radius $\varepsilon \to 0$, to yield $C_1 = (4\pi)^{-1}$. Generalizing the case for $\vec{r}' \neq 0$, r can be replaced by the distance from $\vec{r}'$ to the observation point $\vec{r}$. This gives the 3-D scalar Green's function

$$\hat{G}_A^{3D}(\vec{r}-\vec{r}') = \frac{e^{-i\omega|\vec{r}-\vec{r}'|/c_{A,0}}}{4\pi|\vec{r}-\vec{r}'|}, \tag{A.7}$$

with which equation (2.10) has been derived.

Complex plane derivation

A method to avoid having to disregard a mathematically valid solution, as necessary using the real domain derivation, is by evaluating the integral that is the solution of the spatial Fourier transform of (A.1) in the complex plane. The spatial Fourier transform of (A.1) and its solution are given by

$$-|\vec{k}|^2\tilde{G}_A^{3D} - \gamma^2\tilde{G}_A^{3D} = -1, \tag{A.8}$$

$$\tilde{G}_A^{3D} = \frac{1}{|\vec{k}|^2+\gamma^2}, \tag{A.9}$$

where from now on a tilde, ˜, above a quantity denotes the a temporal and spatial Fourier domain, $\vec{k}$ is the spatial angular wave number and $\gamma = i\frac{\omega}{c_{A,0}} + \delta$, with δ a small real number, which will be needed later on in the derivation to create a complex pole. In the final stage the limit will be taken of $\delta \to 0$, such that $\lim_{\delta\to 0}\gamma^2 = -\frac{\omega^2}{c_{A,0}^2}$. To retrieve $\hat{G}_A^{3D}(\vec{r}-\vec{r}')$, the inverse spatial Fourier transform,

$$\hat{G}_A^{3D}(\vec{r}-\vec{r}') = \frac{1}{(2\pi)^3}\int_V \tilde{G}_A^{3D} e^{-i\vec{k}\cdot(\vec{r}-\vec{r}')} dV(\vec{k}), \tag{A.10}$$

is evaluated. Spherical coordinates are introduced, with $dV(\vec{k}) = |\vec{k}|^2\sin(\theta)d|\vec{k}|d\theta d\phi$ and with limits $0 < |\vec{k}| < \infty$, $0 < \theta < \pi$ and $0 < \phi < 2\pi$. Rewriting the inner product as $\vec{k}\cdot(\vec{r}-\vec{r}') = |\vec{k}||\vec{r}-\vec{r}'|\cos\theta$, the result of the integration over ϕ and θ respectively, is

$$\hat{G}_A^{3D}(\vec{r}-\vec{r}') = \frac{1}{4\pi^2}\int_0^{\infty}\int_0^{\pi} \frac{|\vec{k}|^2\sin\theta}{|\vec{k}|^2+\gamma^2} e^{-i|\vec{k}||\vec{r}-\vec{r}'|\cos\theta} d|\vec{k}|d\theta \tag{A.11}$$

$$= \frac{1}{i4\pi^2|\vec{r}-\vec{r}'|}\int_0^{\infty} \frac{|\vec{k}|}{|\vec{k}|^2+\gamma^2}\left(e^{i|\vec{k}||\vec{r}-\vec{r}'|} - e^{-i|\vec{k}||\vec{r}-\vec{r}'|}\right) d|\vec{k}| \tag{A.12}$$

$$= \frac{1}{i4\pi^2|\vec{r}-\vec{r}'|}\int_{-\infty}^{\infty} \frac{|\vec{k}|}{|\vec{k}|^2+\gamma^2} e^{i|\vec{k}||\vec{r}-\vec{r}'|} d|\vec{k}|, \tag{A.13}$$

where $\frac{d}{d\theta}\frac{e^{-i|\vec{k}||\vec{r}-\vec{r}'|\cos\theta}}{i|\vec{k}||\vec{r}-\vec{r}'|} = \sin\theta e^{-i|\vec{k}||\vec{r}-\vec{r}'|\cos\theta}$ is used to evaluate the integral over θ by means of an anti-derivative, and to yield (A.13) a change of variables and swapping of integration limits is used on

the second term of (A.12).

To evaluate (A.13), a contour integration will be performed in the complex plane, using the complex function $f(z)$,

$$\int_{C_R} f(z)dz = \frac{1}{i4\pi^2|\vec{r}-\vec{r}'|}\int_{C_R}\frac{z}{z^2+\gamma^2}e^{iz|\vec{r}-\vec{r}'|}dz, \tag{A.14}$$

with C_R the closed, positively oriented contour, being the union of the line I_R, the line on the real axis from $-R$ to R, and the semicircle in the upper half plane Γ_R, parametrized by $\Gamma_R = Re^{it}$ with $t \in [0,\pi]$, such that $\int_{C_R} f(z)dz = \int_{I_R} f(z)dz + \int_{\Gamma_R} f(z)dz$, as depicted in Figure A.1. Note that the integral to be evaluated in (A.13) is equal to $\lim_{R\to\infty}\int_{I_R} f(z)dz$.

The contour integrals over C_R and Γ_R will be evaluated separately, starting with C_R. Since C_R is a positively oriented, closed contour, Cauchy's residue theorem can be used to evaluate the integral. The function $f(z)$ in (A.14) has two simple poles, $z_1 = i\gamma$ and $z_2 = -i\gamma$. Since $\gamma = i\omega/c_{A,0} + \delta$ and $\omega > 0, c_{A,0} > 0$ and $\delta > 0$, z_1 lies in the upper left quadrant of the complex plane and z_2 in the lower right quadrant of the complex plane, as shown in Figure A.1. As z_1 is the only pole enclosed by C_R, only the residue of z_1 needs to be evaluated, which is done using the pole theorem. Here $f(z) = p(z)/q(z)$ is used with $p(z) = ze^{iz|\vec{r}-\vec{r}'|}$ and $q(z) = i4\pi^2|\vec{r}-\vec{r}'|(z^2+\gamma^2)$. Because $p(z_1) \neq 0$, $q(z_1) = 0$ and $q'(z_1) \neq 0$, the pole theorem and Cauchy's residue theorem give

$$\int_{C_R} f(z)dz = 2\pi i \operatorname*{Res}_{z_1} f(z) = 2\pi i\frac{p(z_1)}{q'(z_1)} = \frac{e^{-\gamma|\vec{r}-\vec{r}'|}}{4\pi|\vec{r}-\vec{r}'|}. \tag{A.15}$$

To evaluate $\int_{\Gamma_R} f(z)dz$, Jordan's lemma will be used, as the integral is of the form $\int_{\Gamma_R} g(z)e^{iaz}dz$, with $g(z) = z/(i4\pi|\vec{r}-\vec{r}'|(z^2+\gamma^2))$ and $a = |\vec{r}-\vec{r}'|$. The requirements of the lemma: $g(z)$ is analytic in the upper half complex plane exterior to Γ_R, Γ_R is a semicircle parametrized by $\Gamma_R = Re^{it}$ with $t \in [0,\pi]$, $a > 0$ and for all $z \in \Gamma_R$ there is a maximum $M_R > 0$, such that $|g(z)| \leq M_R$ and $\lim_{R\to\infty} M_R = 0$, are met. Here the maximum of $|g(z)|$ on Γ_R is found to be $M_R = \frac{1}{4\pi|\vec{r}-\vec{r}'|}\frac{1/R}{1-|\gamma|^2/R^2}$. Therefore according to Jordan's lemma, the integral over Γ_R in the limit of $R \to \infty$ goes to zero,

$$\lim_{R\to\infty}\int_{\Gamma_R} f(z)dz = 0. \tag{A.16}$$

Now subtracting (A.16) from (A.15) in the limit of $R \to \infty$, the solution to the original integral in equation (A.13) is found. Finally taking the limit of $\delta \to 0$ in $\gamma = i\omega/c_{A,0} + \delta$, the Green's function

$$\hat{G}_A^{3D}(\vec{r}-\vec{r}') = \frac{e^{-i\omega|\vec{r}-\vec{r}'|/c_{A,0}}}{4\pi|\vec{r}-\vec{r}'|}, \tag{A.17}$$

is obtained and we see the result of the real domain derivation (A.7) is reproduced.

A.1.2. Two dimensional case

For the 2-D case, again two different derivations yielding the same result are given, solving the 2-D differential equation (A.1) directly [46] and integrating the 3-D result (A.7) over the z-axis to obtain the 2-D result [48]. A similar derivation in the complex plane as done for the 3-D case is not as simple, since the resulting integral equation is not of the form where Jordan's lemma can be applied and will therefore not be discussed here.

2-D differential equation

Firstly, the 2-D acoustic Green's function can be derived by solving (A.1) directly. Due to circular symmetry and when considering the case $\vec{r} \neq \vec{0}$ and $\vec{r}' = \vec{0}$, equation (A.1) reduces to

$$\frac{d^2\hat{G}_A^{2D}(\vec{r},\vec{0})}{dr^2} + \frac{1}{r}\frac{d\hat{G}_A^{2D}(\vec{r},\vec{0})}{dr} + \frac{\omega^2}{c_{A,0}^2}\hat{G}_A^{2D}(\vec{r},\vec{0}) = 0. \tag{A.18}$$

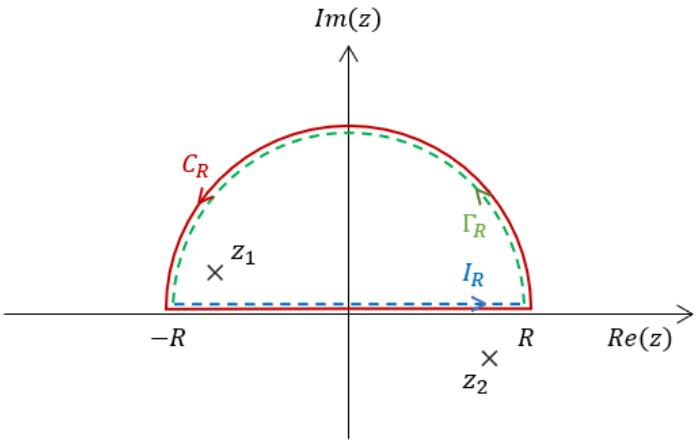

Figure A.1: Complex plane with contours C_R (red), I_R (dashed blue) and Γ_R (dashed green) and the poles $z_1 = i\gamma$ and $z_2 = -i\gamma$.

The solution to this second order ODE is given in terms of the zeroth order Hankel functions of the first and second kind, $H_0^{(1)}$ and $H_0^{(2)}$, respectively,

$$\hat{G}_A^{2D}(\vec{r}, \vec{0}) = C_1 H_0^{(1)}(\omega r/c_{A,0}) + C_2 H_0^{(2)}(\omega r/c_{A,0}), \tag{A.19}$$

where C_1 and C_2 are constants. Since only outgoing waves are considered, C_1 is set to 0. The constant C_2 can be solved to be $C_2 = -i/4$ [46]. This gives the 2-D scalar Green's function in terms of the zeroth order Hankel function of the second kind $H_0^{(2)} = J_0 - iY_0$, for the general case where $\vec{r}' \neq \vec{0}$,

$$\hat{G}_A^{2D}(\vec{r} - \vec{r}') = \frac{-i}{4} H_0^{(2)}(\omega|\vec{r} - \vec{r}'|/c_{A,0}), \tag{A.20}$$

with which equation (2.9) has been derived.

Integration of 3-D result

Another method to derive the Green's function for two dimensions is to convolve the 3-D Green's function with a source that reduces it to two dimensions [48]. This source is located at $(x, y) = (x'', y'')$ and is an infinite line source in the z-direction. The convolution is given by

$$\hat{G}_A^{2D}(\vec{r} - \vec{r}'') = \int_{V'} \delta(x' - x'')\delta(y' - y'')\hat{G}_A^{3D}(\vec{r}_{3D} - \vec{r}'_{3D})dx'dy'dz', \tag{A.21}$$

where in this case $\vec{r} = (x, y)$ is the 2-D position vector and $\vec{r}_{3D} = (x, y, z)$ is the 3-D position vector to make the distinction. Now plugging in the found formulation for $\hat{G}_A^{3D}(\vec{r}_{3D} - \vec{r}'_{3D})$ (A.7), integrating over $dx'dy'$ and letting $\zeta = z - z'$,

$$\hat{G}_A^{2D}(\vec{r} - \vec{r}'') = \frac{1}{4\pi} \int_{-\infty}^{\infty} \frac{e^{-i\omega/c_{A,0}\sqrt{(x-x'')^2+(y-y'')^2+\zeta^2}}}{\sqrt{(x-x'')^2+(y-y'')^2+\zeta^2}} d\zeta, \tag{A.22}$$

is obtained. Using the integral definition of the Hankel function of the first kind [54], and using that for real arguments of the Hankel function $H_0^{(1)}(x) = H_0^{(2)*}(x)$,

$$H_0^{(2)}(kx) = \frac{i}{\pi} \int_{-\infty}^{\infty} \frac{e^{ik\sqrt{x^2+t^2}}}{\sqrt{x^2+t^2}} dt, \tag{A.23}$$

can be compared with equation (A.22), to obtain the final result of the 2-D Green's function

$$\hat{G}_A^{2D}(\vec{r} - \vec{r}') = \frac{-i}{4} H_0^{(2)}(\omega|\vec{r} - \vec{r}'|/c_{A,0}), \tag{A.24}$$

which is the same result as the result in equation (A.20).

A.2. Electromagnetic field

A.2.1. Three dimensional case

For the derivation of the 3-D electromagnetic Green's function [45], the starting point are the Maxwell equations, (2.11-2.14), in the temporal Fourier domain,

$$\nabla \times \hat{\vec{E}}(\vec{r}) = -i\omega\mu_0 \hat{\vec{H}}(\vec{r}), \tag{A.25}$$

$$\nabla \times \hat{\vec{H}}(\vec{r}) = i\omega\epsilon(\vec{r})\hat{\vec{E}}(\vec{r}) + \hat{\vec{J}}^{pr}(\vec{r}), \tag{A.26}$$

$$\nabla \cdot \left[\epsilon(\vec{r})\hat{\vec{E}}(\vec{r})\right] = \hat{\rho}_e^{pr}(\vec{r}) = 0, \tag{A.27}$$

$$\nabla \cdot \left[\mu_0 \hat{\vec{H}}(\vec{r})\right] = 0, \tag{A.28}$$

where $\hat{\vec{E}}(\vec{r})$ is the electric field, $\hat{\vec{H}}(\vec{r})$ the magnetic field, $\hat{\vec{J}}^{pr}(\vec{r})$ the primary electric current density, $\hat{\rho}_e^{pr}(\vec{r})$ the primary electric charge density source, all in the temporal Fourier domain, μ_0 the permeability of the medium and $\epsilon(\vec{r})$ the electric permittivity of the medium at location $\vec{r}$.

The wave equation for electromagnetic waves in the temporal Fourier domain (2.16) can be obtained from (A.25 - A.28), by taking the curl of both sides of (A.25), plugging in (A.26), using the vector calculus identity $\nabla \times (\nabla \times \vec{A}) = \nabla(\nabla \cdot \vec{A}) - \nabla^2 \vec{A}$ and the electromagnetic contrast in (2.17), to yield

$$\nabla^2 \hat{\vec{E}}(\vec{r}) + \frac{\omega^2}{c_{E,0}^2}\hat{\vec{E}}(\vec{r}) = i\omega\mu_0 \hat{\vec{J}}_E^{pr}(\vec{r}) - \omega^2 \chi_E(\vec{r})\hat{\vec{E}}(\vec{r}) + \nabla\left(\nabla \cdot \hat{\vec{E}}(\vec{r})\right), \tag{A.29}$$

with the electromagnetic contrast, $\chi_E(\vec{r}) = c_E^{-2}(\vec{r}) - c_{E,0}^{-2}$, the speed of light at position $\vec{r}$, $c_E(\vec{r})$, and the speed of light of the homogeneous background medium, $c_{E,0}$. The speed of lights are defined by $c_E^{-2}(\vec{r}) = \epsilon(\vec{r})\mu_0$ and $c_{E,0}^{-2} = \epsilon_0\mu_0$, with ϵ_0 the electric permittivity of the homogeneous background medium.

It is important to note that wave equation (A.29) cannot be solved directly using the Green's function from the previous sections, since the vector components of the electric field are not independent and there is a divergence term on the right side. To tackle this, first the wave equation will be split using the fact that the total field can be split into the incident field and the scattered field (2.18). These split wave equations are

$$\nabla^2 \hat{\vec{E}}^{inc}(\vec{r}) + \frac{\omega^2}{c_{E,0}^2}\hat{\vec{E}}^{inc}(\vec{r}) = i\omega\mu_0 \hat{\vec{J}}_E^{pr}(\vec{r}) + \nabla\left(\nabla \cdot \hat{\vec{E}}^{inc}(\vec{r})\right), \tag{A.30}$$

$$\nabla^2 \hat{\vec{E}}^{sct}(\vec{r}) + \frac{\omega^2}{c_{E,0}^2}\hat{\vec{E}}^{sct}(\vec{r}) = -\omega^2 \chi_E(\vec{r})\hat{\vec{E}}(\vec{r}) + \nabla\left(\nabla \cdot \hat{\vec{E}}^{sct}(\vec{r})\right), \tag{A.31}$$

with $\hat{p}^{inc}(\vec{r})$ and $\hat{\vec{E}}^{inc}(\vec{r})$ the incident pressure and electric field, respectively, and $\hat{p}^{sct}(\vec{r})$ and $\hat{\vec{E}}^{sct}(\vec{r})$ the scattered pressure and electric field, respectively. The derivation of the Green's function will be treated separately, starting with the equation for the incident field (A.30).

Incident field

To continue, the Maxwell equations (A.25 - A.28) need to be determined for the wave equation of the incident electric field. By splitting the equations or using the reverse argument which was used to obtain (A.29), the following equations are found for the incident field

$$\nabla \times \hat{\vec{E}}^{inc}(\vec{r}) = -i\omega\mu_0 \hat{\vec{H}}^{inc}(\vec{r}), \tag{A.32}$$

$$\nabla \times \hat{\vec{H}}^{inc}(\vec{r}) = i\omega\epsilon_o \hat{\vec{E}}^{inc}(\vec{r}) + \hat{\vec{J}}^{pr}(\vec{r}), \tag{A.33}$$

$$\nabla \cdot \left[\epsilon_0 \hat{\vec{E}}^{inc}(\vec{r})\right] = \hat{\rho}_e^{pr}(\vec{r}) = 0, \tag{A.34}$$

$$\nabla \cdot \left[\mu_0 \hat{\vec{H}}^{inc}(\vec{r})\right] = 0, \tag{A.35}$$

with $\hat{\vec{H}}^{inc}(\vec{r})$ the incident magnetic field. To keep the analogy with the acoustic waves, an analogous

vector Helmholtz equation is to be found. To get here, it is required to introduce the vector potential $\vec{\hat{A}}^{inc}(\vec{r})$ and the scalar potential $\hat{\phi}^{inc}(\vec{r})$. Using the vector calculus identity, $\nabla \cdot (\nabla \times \vec{A}) = 0$, and equation (A.35), the vector potential can be introduced as

$$\nabla \times \vec{\hat{A}}^{inc}(\vec{r}) = \vec{\hat{H}}^{inc}(\vec{r}). \tag{A.36}$$

Now substituting (A.36) into (A.32) yields

$$\nabla \times \left(\vec{\hat{E}}^{inc}(\vec{r}) + i\omega\mu_0 \vec{\hat{A}}^{inc}(\vec{r}) \right) = 0. \tag{A.37}$$

Next, the scalar potential can be introduced using the vector calculus identity, $\nabla \times (\nabla \phi) = 0$, and equation (A.37), such that

$$\vec{\hat{E}}^{inc}(\vec{r}) + i\omega\mu_0 \vec{\hat{A}}^{inc}(\vec{r}) = -\nabla \hat{\phi}^{inc}(\vec{r}). \tag{A.38}$$

Now to satisfy equation (A.33), equations (A.36) and (A.38) are substituted into it to obtain

$$\nabla \times \left(\nabla \times \vec{\hat{A}}^{inc}(\vec{r}) \right) = -i\omega\epsilon_0 \nabla \hat{\phi}^{inc}(\vec{r}) + \frac{\omega^2}{c_{E,0}^2} \vec{\hat{A}}^{inc}(\vec{r}) + \vec{\hat{J}}^{pr}(\vec{r}). \tag{A.39}$$

By rearranging and using the vector calculus identity $\nabla \times (\nabla \times \vec{A}) = \nabla(\nabla \cdot \vec{A}) - \nabla^2 \vec{A}$, this is reduced to

$$\nabla \left(\nabla \cdot \vec{\hat{A}}^{inc}(\vec{r}) \right) - \nabla^2 \vec{\hat{A}}^{inc}(\vec{r}) = -i\omega\epsilon_0 \nabla \hat{\phi}^{inc}(\vec{r}) + \frac{\omega^2}{c_{E,0}^2} \vec{\hat{A}}^{inc}(\vec{r}) + \vec{\hat{J}}^{pr}(\vec{r}). \tag{A.40}$$

Since the divergence of the vector potential has not been set yet, equation (A.40) can be simplified by using the Lorenz gauge condition,

$$\nabla \cdot \vec{\hat{A}}^{inc}(\vec{r}) = -i\omega\epsilon_0 \hat{\phi}^{inc}(\vec{r}), \tag{A.41}$$

such that equation (A.40) reduces to

$$\nabla^2 \vec{\hat{A}}^{inc}(\vec{r}) + \frac{\omega^2}{c_{E,0}^2} \vec{\hat{A}}^{inc}(\vec{r}) = -\vec{\hat{J}}^{pr}(\vec{r}), \tag{A.42}$$

which is the vector Helmholtz equation. This second order partial differential equation is linear, that is it can be expressed as the linear superposition of the solutions due to point sources, which is the 3-D Green's function (A.7) as discussed in the previous section. This gives

$$\vec{\hat{A}}^{inc}(\vec{r}) = \int_{\vec{r}' \in \mathbb{D}} \hat{G}^{3D}(\vec{r} - \vec{r}') \vec{\hat{J}}^{pr}(\vec{r}') dV(\vec{r}'). \tag{A.43}$$

Substituting (A.41) into (A.38), the equation to determine $\vec{\hat{E}}^{inc}(\vec{r})$ from $\vec{\hat{A}}^{inc}(\vec{r})$ is obtained,

$$\vec{\hat{E}}^{inc}(\vec{r}) = -i\omega\mu_0 \vec{\hat{A}}^{inc}(\vec{r}) + \frac{1}{i\omega\epsilon_0} \nabla \left(\nabla \cdot \vec{\hat{A}}^{inc}(\vec{r}) \right). \tag{A.44}$$

Inserting (A.43) into (A.44), the electric incident field integral equation,

$$\vec{\hat{E}}^{inc}(\vec{r}) = -i\omega\mu_0 \int_{\vec{r}' \in \mathbb{D}} \left[1 + \frac{c_{E,0}^2}{\omega^2} \nabla\nabla\cdot \right] \hat{G}^{3D}(\vec{r} - \vec{r}') \vec{\hat{J}}^{pr}(\vec{r}') dV(\vec{r}'), \tag{A.45}$$

is obtained. This can be simplified to

$$\vec{\hat{E}}^{inc}(\vec{r}) = \int_{\vec{r}' \in \mathbb{D}} \hat{G}_E^{3D}(\vec{r} - \vec{r}') \vec{\hat{S}}_E^{pr}(\vec{r}') dV(\vec{r}'), \tag{A.46}$$

with primary source term of the electric field $\vec{\hat{S}}_E^{pr}(\vec{r}) = -i\omega\mu_0 \vec{\hat{J}}^{pr}(\vec{r})$, such that (2.19) is reproduced.

Scattered field

Now a similar procedure will be followed, starting from the wave equation for the scattered field (A.30). The Maxwell equations leading to this wave equations are

$$\nabla \times \vec{\hat{E}}^{sct}(\vec{r}) = -i\omega\mu_0 \vec{\hat{H}}^{sct}(\vec{r}), \tag{A.47}$$

$$\nabla \times \vec{\hat{H}}^{sct}(\vec{r}) = i\omega\epsilon_0 \vec{\hat{E}}^{sct}(\vec{r}) + i\omega(\epsilon(\vec{r}) - \epsilon_0)\vec{\hat{E}}(\vec{r}), \tag{A.48}$$

$$\nabla \cdot \left[\epsilon(\vec{r})\vec{\hat{E}}^{sct}(\vec{r})\right] = \hat{\rho}_e^{pr}(\vec{r}) = 0, \tag{A.49}$$

$$\nabla \cdot \left[\mu_0 \vec{\hat{H}}^{sct}(\vec{r})\right] = 0, \tag{A.50}$$

with $\vec{\hat{H}}^{sct}(\vec{r})$ the scattered magnetic field. Again a vector potential $\vec{\hat{A}}^{sct}(\vec{r})$ and a scalar potential $\hat{\phi}^{sct(\vec{r})}$ will be introduced. As for the vector potential, the vector calculus identity $\nabla \cdot (\nabla \times \vec{A}) = 0$, and equation (A.50) are used to obtain

$$\nabla \times \vec{\hat{A}}^{sct}(\vec{r}) = \vec{\hat{H}}^{sct}(\vec{r}). \tag{A.51}$$

Next, (A.51) is substituted into (A.47),

$$\nabla \times \left(\vec{\hat{E}}^{sct}(\vec{r}) + i\omega\mu_0 \vec{\hat{A}}^{sct}(\vec{r})\right) = 0. \tag{A.52}$$

Now the scalar potential function for the scattered field can be introduced, by combining equation (A.52) and the identity $\nabla \times (\nabla\phi) = 0$, as

$$\vec{\hat{E}}^{sct}(\vec{r}) + i\omega\mu_0 \vec{\hat{A}}^{sct}(\vec{r}) = -\nabla\hat{\phi}^{sct}(\vec{r}). \tag{A.53}$$

To satisfy (A.48), equations (A.51) and (A.53) are plugged in to obtain

$$\nabla \times (\nabla \times \vec{\hat{A}}^{sct}) = -i\omega\epsilon_0 \nabla\hat{\phi}^{sct}(\vec{r}) + \frac{\omega^2}{c_0^2}\vec{\hat{A}}^{sct}(\vec{r}) + i\omega(\epsilon(\vec{r}) - \epsilon_0)\vec{\hat{E}}(\vec{r}). \tag{A.54}$$

Using vector calculus identity $\nabla \times (\nabla \times \vec{A}) = \nabla(\nabla \cdot \vec{A} - \nabla^2\vec{A})$, (A.54) becomes

$$\nabla\left(\nabla \cdot \vec{\hat{A}}^{sct}(\vec{r})\right) - \nabla^2\vec{\hat{A}}^{sct}(\vec{r}) = -i\omega\epsilon_0 \nabla\hat{\phi}^{sct}(\vec{r}) + \frac{\omega^2}{c_0^2}\vec{\hat{A}}^{sct}(\vec{r}) + i\omega(\epsilon(\vec{r}) - \epsilon_0)\vec{\hat{E}}(\vec{r}). \tag{A.55}$$

The divergence of the vector potential is set by the Lorenz gauge,

$$\nabla \cdot \vec{\hat{A}}^{sct}(\vec{r}) = -i\omega\epsilon_0 \hat{\phi}^{sct}(\vec{r}), \tag{A.56}$$

which can be substituted into (A.55) to yield the vector Helmholtz equation for the scattered vector potential

$$\nabla^2\vec{\hat{A}}^{sct}(\vec{r}) + \frac{\omega^2}{c_0^2}\vec{\hat{A}}^{sct}(\vec{r}) = -i\omega(\epsilon(\vec{r}) - \epsilon_0)\vec{\hat{E}}(\vec{r}). \tag{A.57}$$

The solution to this second order partial differential equation is the convolution of the 3-D Green's function (A.7) with the term on the right side of (A.57), which is

$$\vec{\hat{A}}^{sct}(\vec{r}) = i\omega \int_{\vec{r}' \in \mathbb{D}} \hat{G}^{3D}(\vec{r} - \vec{r}')\left[\epsilon(\vec{r}') - \epsilon_0\right]\vec{\hat{E}}(\vec{r}')dV(\vec{r}'). \tag{A.58}$$

Substituting (A.56) into (A.53), $\vec{\hat{E}}^{sct}(\vec{r})$ can be expressed in terms of $\vec{\hat{A}}^{sct}(\vec{r})$

$$\vec{\hat{E}}^{sct}(\vec{r}) = -i\omega\mu_0 \vec{\hat{A}}^{sct}(\vec{r}) + \frac{1}{i\omega\epsilon_0}\nabla\left(\nabla \cdot \vec{\hat{A}}^{sct}(\vec{r})\right). \tag{A.59}$$

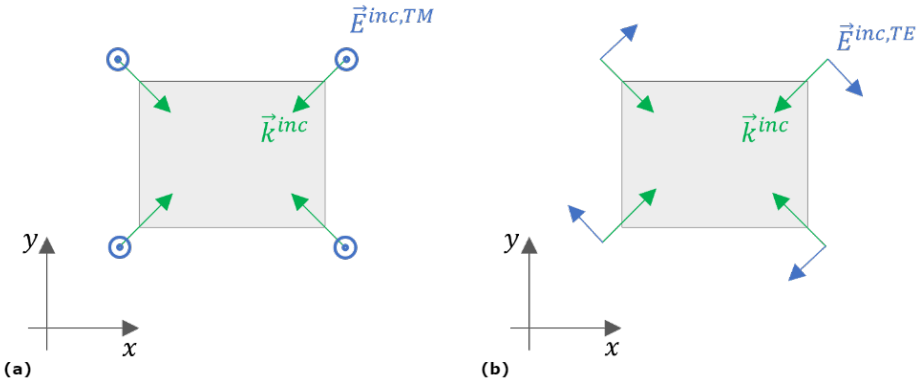

Figure A.2: Schematic representation of four TM and TE waves propagating into the imaged 2-D surface in the (x,y)-plane (gray surface), $\vec{E}^{inc}$ (blue arrow) the incident electric field and $\vec{k}^{inc}$ (green arrow) the incident wave vector representing the direction of propagation. (a) TM waves, with electric field completely perpendicular tot the surface, (b) TE waves, with electric field completely parallel to the surface.

Inserting (A.58) into (A.59), the electric scattered field integral equation,

$$\hat{\vec{E}}^{sct}(\vec{r}) = \omega^2 \int_{\vec{r}'\in\mathbb{D}} \left[1 + \frac{c_{E,0}^2}{\omega^2}\nabla\nabla\cdot\right] \hat{G}^{3D}(\vec{r}-\vec{r}')\chi_E(\vec{r}')\hat{\vec{E}}(\vec{r}')dV(\vec{r}'), \tag{A.60}$$

is obtained. This can be simplified to

$$\hat{\vec{E}}^{sct}(\vec{r}) = \omega^2 \int_{\vec{r}'\in\mathbb{D}} \hat{G}_E^{3D}(\vec{r}-\vec{r}')\chi_E(\vec{r}')\hat{\vec{E}}(\vec{r}')dV(\vec{r}'), \tag{A.61}$$

such that (2.20) is reproduced.

3-D electromagnetic Green's function
Finally, it can be seen that from both the integral equation of the incident field (A.45) and (A.46) and the integral equation of the scattered field (A.60) and (A.61) the expression for the 3-D Green's function for the electric field can be written as

$$\hat{G}_E^{3D}(\vec{r}-\vec{r}') = \left(1 + \frac{c_{E,0}^2}{\omega^2}\nabla\nabla\cdot\right)\frac{e^{-i\omega|\vec{r}-\vec{r}'|/c_{E,0}}}{4\pi|\vec{r}-\vec{r}'|}, \tag{A.62}$$

which is equal to equation (2.23).

A.2.2. Two dimensional case

For the 2-D electromagnetic case, the derivation of the Green's function is for the largest part equal to that of the 3-D case. In particular, one method to obtain it, is integrating the 3-D result over the z-axis, like has been done for the acoustic 2-D Green's function.

The same result can be obtained when considering the Maxwell equations in two spatial dimensions [50, 51]. In this case, the vector calculus must change. When an outer product is involved, $\vec{A}\times\vec{B}$ will be written in the 2-D case as $\vec{A}_\perp\cdot\vec{B}$, with $\vec{A}_\perp = (A_y, -A_x)$. Accordingly the differential operator in two dimensions is written as $\nabla = (\partial/\partial x, \partial/\partial y)$, the curl will be replaced by $\nabla_\perp = (\partial/\partial y, -\partial/\partial x)$, the Laplacian by $\nabla^2 = \nabla\cdot\nabla = \nabla_\perp\cdot\nabla_\perp = (\partial^2/\partial x^2, \partial^2/\partial y^2)$ and finally the vector calculus identity of the curl of a curl will be $\nabla_\perp(\nabla_\perp\cdot\vec{A}) = \nabla^2\vec{A} - \nabla(\nabla\cdot\vec{A})$. Using this vector calculus, the derivation of the 2-D Green's function of the electromagnetic field is completely analogous to the derivation of the 3-D Green's function. However, in 2-D one can distinguish transverse magnetic (TM) and transverse electric (TE) waves, of which the geometries are shown in Figure A.2. First the derivation of the TM case is discussed, followed by a discussion of the TE case.

TM waves

In the case of TM waves, the magnetic field is transverse to the vector that describes the imaged plane, i.e. the normal [30], [43]. This means, the incident magnetic field is completely parallel to the imaged plane, and the incident electric field is completely perpendicular to the imaged 2-D surface, as shown in Figure A.2(a). In other words, the electric field no longer has a direction into the 2-D surface, as it points in the z-direction. From (A.32) and (A.36), it can be seen that $\vec{\hat{A}}^{inc}(\vec{r})$ is parallel to $\vec{\hat{E}}^{inc}(\vec{r})$. The 2-D divergence of $\vec{\hat{A}}^{inc}(\vec{r})$ is therefore zero. This means, that for the 2-D TM case, equation (A.44) reduces to

$$\vec{\hat{E}}^{inc}(\vec{r}) = -i\omega\mu_0 \vec{\hat{A}}^{inc}(\vec{r}). \tag{A.63}$$

Note that in (A.63) the electric field and the vector potential are still written in vector notation, but that the direction in the 2-D plane in this case has no definition, not containing a z-direction. Now continuing with the derivation, (A.43) is inserted into (A.63), yielding

$$\vec{\hat{E}}(\vec{r}) = \int_{\vec{r}' \in \mathbb{D}} \hat{G}^{2D}(\vec{r} - \vec{r}') \left(-i\omega\mu_0 \vec{\hat{f}}^{pr}(\vec{r}') \right) dA(\vec{r}'), \tag{A.64}$$

where $-i\omega\mu_0 \vec{\hat{f}}^{pr}(\vec{r})$ is the source term $\vec{\hat{S}}_E^{pr}(\vec{r})$, with $\vec{\hat{f}}^{pr}(\vec{r})$ and therefore $\vec{\hat{S}}_E^{pr}(\vec{r}')$ pointing in the z-direction in the 2-D TM case, as they are parallel to $\vec{\hat{E}}(\vec{r})$. Equation (A.64) shows the 2-D electromagnetic Green's function for the TM case is identical to the 2-D acoustic Green's function and therefore is

$$\hat{G}_E^{2D,TM}(\vec{r} - \vec{r}') = \frac{-i}{4} H_0^{(2)}(\omega|\vec{r} - \vec{r}'|/c_{E,0}). \tag{A.65}$$

TE waves

The case of TE waves is shown in Figure A.2(b). Here, the incident electric field is transverse to the normal vector of the imaged plane, or, in other words, parallel to the imaged 2-D surface. Now the electric field only has x- and y-components. As the divergence term in (A.44) will not be zero, the derivation of the 2-D electromagnetic Green's function for the TE case remains completely identical to the 3-D electromagnetic case, except for replacing the scalar 3-D Green's function by the scalar 2-D Green's function, to finally yield

$$\hat{G}_E^{2D,TE}(\vec{r} - \vec{r}') = \left(1 + \frac{c_{E,0}^2}{\omega^2} \nabla\nabla\cdot \right) \frac{-i}{4} H_0^{(2)}(\omega|\vec{r} - \vec{r}'|/c_{E,0}). \tag{A.66}$$

B

Derivation update direction and amplitude joint inversion

This appendix holds the derivation of the minimization of the error functions for the joint inversion, to find the update directions, $d_A^{(n)}$ and $d_E^{(n)}$ and the corresponding amplitudes, $\alpha_A^{(n)}$ and $\alpha_E^{(n)}$, of both contrasts at the n-th iteration, as given by

$$\chi_A^{(n)} = \chi_A^{(n-1)} + \alpha_A^{(n)} d_A^{(n)}, \tag{B.1}$$

$$\chi_E^{(n)} = \chi_E^{(n-1)} + \alpha_E^{(n)} d_E^{(n)}, \tag{B.2}$$

where $\chi_A^{(n)}$ is the acoustic contrast at the n-th iteration and $\chi_E^{(n)}$ the electromagnetic contrast at the n-th iteration. The corresponding separate residuals at the n-th iteration, $r_A^{(n)}$ and $r_E^{(n)}$ are given by

$$r_A^{(n)} = \hat{p}^{meas} - \mathrm{L_A}\chi_A^{(n)}, \tag{B.3}$$

$$r_E^{(n)} = \vec{\hat{E}}^{meas} - \mathrm{L_E}\chi_E^{(n)}, \tag{B.4}$$

with $\mathrm{L_A}$ the acoustic operator given by $\mathrm{L_A}\chi_A^{(n)} = \hat{G}_A * (\omega^2 \hat{p}^{inc}\chi_A^{(n)})$ and $\mathrm{L_E}$ the electromagnetic operator given by $\mathrm{L_E}\chi_E^{(n)} = \hat{G}_E * (\omega^2 \vec{\hat{E}}^{inc}\chi_E^{(n)})$, where ω is the angular frequency, $\hat{G}_A$ and $\hat{G}_E$ the acoustic and electromagnetic Green's functions, $*$ the spatial convolution operator and, $\hat{p}^{meas}$ and $\vec{\hat{E}}^{meas}$ the measured pressure and electric field, respectively. Note that from here and onward, the caret symbol, ^, is used to denote quantities in the temporal Fourier domain, with the used definition of the Fourier transform $\hat{p}(\vec{r}) = \int_{-\infty}^{\infty} p(\vec{r}, t) e^{i\omega t} dt$.

First the derivation is given for the cross-gradient approach (CG), the acoustic and electromagnetic case treated subsequently, next, the derivation for the gradient difference (GD) approach is shown.

B.1. Cross-gradient approach

Within this section the derivation of the update direction and the update amplitude is shown for the CG constraint. In the developed algorithm, the acoustic contrast will be updated first, followed by the electromagnetic contrast. Therefore, the electromagnetic derivation will follow after the acoustic derivation of the update parameters.

B.1.1. Acoustic field

The additive acoustic error function, $Err_A^{(n)}$, to be minimized at the n-th iteration is

$$Err_A^{(n)} = Err_{A,BI}^{(n)} + Err_{A,CG}^{(n)} = \frac{||\hat{p}^{meas} - \mathrm{L_A}\chi_A^{(n)}||^2}{||\hat{p}^{meas}||^2} + \beta_A \frac{||\nabla\chi_A^{(n)} \times \nabla\chi_E^{(n-1)}||^2}{||\nabla\chi_A^{(n-1)} \times \nabla\chi_E^{(n-1)}||^2}, \tag{B.5}$$

where $Err_{A,BI}^{(n)}$ is the contribution as seen in separate Born inversion, $Err_{A,CG}^{(n)}$ the contribution due to the joint structural constraint by the CG term, $\hat{p}^{meas}$ the measured scattered field and β_A the acoustic regularization parameter for the joint inversion. The location dependencies of $\hat{p}^{meas}$, χ_A and χ_E are left out for simplicity. Note that within the numerator of $Err_{A,CG}^{(n)}$ the electromagnetic contrast for the $(n-1)$-th iteration is used, as the acoustic contrast is updated first.

Update direction

To find the update direction of the acoustic contrast, a Fréchet derivative of error function (B.5) can be used, finding the steepest negative direction. This will be done for both terms separately. For the $Err_{A,BI}^{(n)}$ we have:

$$\frac{\partial Err_{A,BI}^{(n)}}{\partial \chi_A^{(n)}} = \frac{1}{||\hat{p}^{meas}||^2} \lim_{\varepsilon \to 0} \left[\frac{||\hat{p}^{meas} - \mathrm{L_A}\left(\chi_A^{(n-1)} + \varepsilon d_{A,BI}^{(n)}\right)||^2 - ||\hat{p}^{meas} - \mathrm{L_A}\chi_A^{(n-1)}||^2}{\varepsilon} \right], \tag{B.6}$$

where ε is a small real number and $d_{A,BI}^{(n)}$ is the contribution of $Err_{A,BI}^{(n)}$ to the update direction $d_A^{(n)}$ in equation (B.1). Equation (B.6) can be reduced by expanding the brackets and square terms, taking the acoustic operator to the other side of the inner product, using equation (B.3) and finally taking the limit of $\varepsilon \to 0$, to yield

$$\frac{\partial Err_{A,BI}^{(n)}}{\partial \chi_A^{(n)}} = \frac{1}{||\hat{p}^{meas}||^2} \lim_{\varepsilon \to 0} \left[\frac{||r_A^{(n-1)}||^2 + \varepsilon^2 ||\mathrm{L_A} d_{A,BI}^{(n)}||^2 - 2\varepsilon \mathrm{Re} < r_A^{(n-1)}, \mathrm{L_A} d_{A,BI}^{(n)} > - ||r_A^{(n-1)}||^2}{\varepsilon} \right] \tag{B.7}$$

$$= \frac{1}{||\hat{p}^{meas}||^2} \lim_{\varepsilon \to 0} \left[\varepsilon ||\mathrm{L_A} d_{A,BI}^{(n)}||^2 - 2\mathrm{Re} < \mathrm{L_A^\dagger} r_A^{(n-1)}, d_{A,BI}^{(n)} > \right] \tag{B.8}$$

$$= \frac{-2\mathrm{Re} < \mathrm{L_A^\dagger} r_A^{(n-1)}, d_{A,BI}^{(n)} >}{||\hat{p}^{meas}||^2}, \tag{B.9}$$

In order to minimize equation (B.9), the inner product of $\mathrm{L_A^\dagger} r_A^{(n-1)}$ and $d_{A,BI}^{(n)}$ is to be maximized. This is achieved when $\mathrm{L_A^\dagger} r_A^{(n-1)}$ and $d_{A,BI}^{(n)}$ are parallel. Thus for $d_{A,BI}^{(n)}$ the following expression is found,

$$d_{A,BI}^{(n)} = \mathrm{L_A^\dagger} r_A^{(n-1)}. \tag{B.10}$$

The Fréchet derivative of the second term in equation (B.5), $Err_{A,CG}^{(n)}$, is given by

$$\frac{\partial Err_{A,CG}^{(n)}}{\partial \chi_A^{(n)}} = \frac{\beta_A}{||\nabla \chi_A^{(n-1)} \times \nabla \chi_E^{(n-1)}||^2} \lim_{\varepsilon \to 0} \left[\frac{||\nabla \left(\chi_A^{(n-1)} + \varepsilon d_{A,CG}^{(n)}\right) \times \nabla \chi_E^{(n-1)}||^2 - ||\nabla \chi_A^{(n-1)} \times \nabla \chi_E^{(n-1)}||^2}{\varepsilon} \right], \tag{B.11}$$

where ε is again a small, real number and $d_{A,CG}^{(n)}$ is the contribution of $Err_{A,CG}^{(n)}$ to the update direction $d_A^{(n)}$ in (B.1). By expanding the brackets, expanding the square terms and taking the limit of $\varepsilon \to 0$, equation (B.11) is reduced to

$$\frac{\partial Err_{A,CG}^{(n)}}{\partial \chi_A^{(n)}} = \frac{\beta_A}{||\nabla \chi_A^{(n-1)} \times \nabla \chi_E^{(n-1)}||^2} \lim_{2\varepsilon \to 0} \left[\frac{||\nabla \chi_A^{(n-1)} \times \nabla \chi_E^{(n-1)} + \varepsilon \nabla d_{A,CG}^{(n)} \times \nabla \chi_E^{(n-1)}||^2 - ||\nabla \chi_A^{(n-1)} \times \nabla \chi_E^{(n-1)}||^2}{\varepsilon} \right] \tag{B.12}$$

$$= \frac{\beta_A}{||\nabla \chi_A^{(n-1)} \times \nabla \chi_E^{(n-1)}||^2} \lim_{2\varepsilon \to 0} \left[\varepsilon ||\nabla d_{A,CG}^{(n)} \times \nabla \chi_E^{(n-1)}||^2 + 2\mathrm{Re} < d_{A,CG}^{(n)} \times \nabla \chi_E^{(n-1)}, \nabla \chi_A^{(n-1)} \times \nabla \chi_E^{(n-1)} > \right] \tag{B.13}$$

$$= \frac{2\beta_A \mathrm{Re} < \nabla d_{A,CG}^{(n)} \times \nabla \chi_E^{(n-1)}, \nabla \chi_A^{(n-1)} \times \nabla \chi_E^{(n-1)} >}{||\nabla \chi_A^{(n-1)} \times \nabla \chi_E^{(n-1)}||^2} \tag{B.14}$$

$$= \frac{2\beta_A \mathrm{Re} < \nabla d^{(n)} \times \vec{e}^{(n-1)}, \vec{b}^{(n-1)} >}{||\vec{b}^{(n-1)}||^2}, \tag{B.15}$$

where in (B.15) $d^{(n)} = d_{A,CG}^{(n)}$, $\vec{e}^{(n)} = \nabla\chi_E^{(n)}$ and $\vec{b}^{(n)} = \nabla\chi_A^{(n)} \times \nabla\chi_E^{(n)}$ to simplify the expressions in the rest of the derivation. Next, the inner product in equation (B.15) is rewritten to the integral form, and the vector calculus identity $(\nabla\phi) \times \vec{A} = \nabla \times (\phi\vec{A}) - \phi(\nabla \times \vec{A})$ is used to obtain

$$\frac{\partial Err_{A,CG}^{(n)}}{\partial \chi_A^{(n)}} = \frac{2\beta_A}{||\vec{b}^{(n-1)}||^2}\mathrm{Re}\int_V \left(\nabla \times \left(d^{(n)}\vec{e}^{(n-1)}\right)\right) \cdot \vec{b}^{(n-1)*} - d^{(n)}\left(\nabla \times \vec{e}^{(n-1)}\right) \cdot \vec{b}^{(n-1)*} dV. \tag{B.16}$$

Next, the vector calculus identity $\nabla \cdot (\vec{A} \times \vec{B}) = (\nabla \times \vec{A}) \cdot \vec{B} - (\nabla \times \vec{B}) \cdot \vec{A}$ is used in the first term on the right-hand side of (B.16) and subsequently Gauss' theorem is applied to yield

$$\frac{\partial Err_{A,CG}^{(n)}}{\partial \chi_A^{(n)}} = \frac{2\beta_A}{||\vec{b}^{(n-1)}||^2}\mathrm{Re}\int_V \nabla \cdot \left(\left(d^{(n)}\vec{e}^{(n-1)}\right) \times \vec{b}^{(n-1)*}\right) + \left(\nabla \times \vec{b}^{(n-1)*}\right) \cdot d^{(n)}\vec{e}^{(n-1)} - d^{(n)}\left(\nabla \times \vec{e}^{(n-1)}\right) \cdot \vec{b}^{(n-1)*} dV \tag{B.17}$$

$$= \frac{2\beta_A}{||\vec{b}^{(n-1)}||^2}\mathrm{Re}\left[\int_{\partial V} d^{(n)}\left(\vec{e}^{(n-1)}\right) \times \vec{b}^{(n-1)*} dS + \int_V d^{(n)}\left(\nabla \times \vec{b}^{(n-1)*}\right) \cdot \vec{e}^{(n-1)} - d^{(n)}\left(\nabla \times \vec{e}^{(n-1)}\right) \cdot \vec{b}^{(n-1)*} dV\right]. \tag{B.18}$$

Since all terms in the surface integral consist of contrasts, and the contrasts are assumed to be zero on the boundary, this term vanishes. On the remaining volume integral the same vector calculus identity as before, $\nabla \cdot (\vec{A} \times \vec{B}) = \left(\nabla \times \vec{A}\right) \cdot \vec{B} - (\nabla \times \vec{B}) \cdot \vec{A}$, can be applied to result in

$$\frac{\partial Err_{A,CG}^{(n)}}{\partial \chi_A^{(n)}} = \frac{-2\beta_A \mathrm{Re}\int_V d^{(n)}\nabla \cdot \left(\vec{e}^{(n-1)} \times \vec{b}^{(n-1)*}\right) dV}{||\vec{b}^{(n-1)}||^2}. \tag{B.19}$$

To minimize this result, $d^{(n)}$ should be parallel to $\nabla \cdot \left(\vec{e}^{(n-1)*} \times \vec{b}^{(n-1)}\right)$, which gives

$$d_{A,CG}^{(n)} = \nabla \cdot \left[\nabla\chi_E^{(n-1)*} \times \left(\nabla\chi_A^{(n-1)} \times \nabla\chi_E^{(n-1)}\right)\right]. \tag{B.20}$$

Finally, the total update direction of the acoustic contrast is given by

$$d_A^{(n)} = d_{A,BI}^{(n)} + d_{A,CG}^{(n)} = \mathrm{L_A^\dagger} r_A^{(n-1)} + \nabla \cdot \left[\nabla\chi_E^{(n-1)*} \times \left(\nabla\chi_A^{(n-1)} \times \nabla\chi_E^{(n-1)}\right)\right]. \tag{B.21}$$

Update amplitude

To find the update amplitude of the acoustic contrast, $\alpha_A^{(n)}$, in equation (B.1), error function (B.5) is minimized with respect to $\alpha_A^{(n)}$. In order to do this, the error function first needs to be rewritten, starting by plugging in equation (B.1), to obtain

$$Err_A^{(n)} = \frac{||\hat{p}^{meas} - \mathrm{L_A}\left(\chi_A^{(n-1)} + \alpha_A^{(n)}d_A^{(n)}\right)||^2}{||\hat{p}^{meas}||^2} + \beta_A \frac{||\nabla\left(\chi_A^{(n-1)} + \alpha_A^{(n)}d_A^{(n)}\right) \times \nabla\chi_E^{(n-1)}||^2}{||\nabla\chi_A^{(n-1)} \times \nabla\chi_E^{(n-1)}||^2}. \tag{B.22}$$

Next, by expanding the brackets and square terms and using the residual in (B.3), equation (B.22) becomes

$$Err_A^{(n)} = \frac{||r_A^{(n-1)}||^2 + \alpha_A^{(n)2}||\mathrm{L_A}d_A^{(n)}||^2 - 2\alpha_A^{(n)}\mathrm{Re}\,< r_A^{(n-1)}, \mathrm{L_A}d_A^{(n)} >}{||\hat{p}^{meas}||^2} + \tag{B.23}$$

$$\beta_A \frac{||\nabla\chi_A^{(n-1)} \times \nabla\chi_E^{(n-1)}||^2 + \alpha_A^{(n)2}||\nabla d_A^{(n)} \times \nabla\chi_E^{(n-1)}||^2 + 2\alpha_A^{(n)}\mathrm{Re} < \nabla\chi_A^{(n-1)} \times \nabla\chi_E^{(n-1)}, \nabla d_A^{(n)} \times \nabla\chi_E^{(n-1)} >}{||\nabla\chi_A^{(n-1)} \times \nabla\chi_E^{(n-1)}||^2}.$$

Now, the error (B.23) is minimized with respect to $\alpha_A^{(n)}$,

$$\frac{\partial Err_A^{(n)}}{\partial \alpha_A^{(n)}} = \frac{2\alpha_A^{(n)}||\mathrm{L_A}d_A^{(n)}||^2 - 2\mathrm{Re} < r_A^{(n-1)}, \mathrm{L_A}d_A^{(n)} >}{||\hat{p}^{meas}||^2} +$$

$$\beta_A \frac{2\alpha_A^{(n)}||\nabla d_A^{(n)} \times \nabla\chi_E^{(n-1)}||^2 + 2\mathrm{Re} < \nabla\chi_A^{(n-1)} \times \nabla\chi_E^{(n-1)}, \nabla d_A^{(n)} \times \nabla\chi_E^{(n-1)} >}{||\nabla\chi_A^{(n-1)} \times \nabla\chi_E^{(n-1)}||^2} = 0. \tag{B.24}$$

Reordering the terms, $\alpha_A^{(n)}$ is found to be

$$\alpha_A^{(n)} = \frac{\mathrm{Re}<r_A^{(n-1)}, \mathrm{L_A} d_A^{(n)}> ||\nabla\chi_A^{(n-1)} \times \nabla\chi_E^{(n-1)}||^2 - \beta_A \mathrm{Re}<\nabla\chi_A^{(n-1)} \times \nabla\chi_E^{(n-1)}, \nabla d_A^{(n)} \times \nabla\chi_E^{(n-1)}> ||\hat{p}^{meas}||^2}{||\mathrm{L_A} d_A^{(n)}||^2 ||\nabla\chi_A^{(n-1)} \times \nabla\chi_E^{(n-1)}||^2 + \beta_A ||\nabla d_A^{(n)} \times \nabla\chi_E^{(n-1)}||^2 ||\hat{p}^{meas}||^2}. \quad \text{(B.25)}$$

B.1.2. Electromagnetic field

For the electromagnetic case, the additive error function, $Err_E^{(n)}$, to be minimized at the n-th iteration is

$$Err_E^{(n)} = Err_{E,BI}^{(n)} + Err_{E,CG}^{(n)} = \frac{||\vec{\hat{E}}^{meas} - \mathrm{L_E}\chi_E^{(n)}||^2}{||\vec{\hat{E}}^{meas}||^2} + \beta_E \frac{||\nabla\chi_A^{(n)} \times \nabla\chi_E^{(n)}||^2}{||\nabla\chi_A^{(n-1)} \times \nabla\chi_E^{(n-1)}||^2}, \quad \text{(B.26)}$$

where $Err_{E,BI}^{(n)}$ is the contribution as seen in separate Born inversion, $Err_{E,CG}^{(n)}$ the contribution due to the joint CG constraint, $\vec{\hat{E}}^{meas}$ the measured scattered electric field and β_E the electromagnetic regularization parameter for joint inversion. The location dependencies of $\vec{\hat{E}}^{meas}$, χ_A and χ_E are left out for simplicity. Finally, note that within the numerator of $Err_{E,CG}^{(n)}$, the acoustic contrast or the n-th iteration is used, as it was updated before the electromagnetic contrast.

Update direction

Similarly as in the acoustic derivation, the update direction of the electromagnetic contrast can be found using a Fréchet derivative on the error function (B.26), to find the steepest negative direction, for both terms separately. For the first term, $Err_{E,BI}^{(n)}$ this gives,

$$\frac{\partial Err_{E,BI}^{(n)}}{\partial \chi_E^{(n)}} = \frac{1}{||\vec{\hat{E}}^{meas}||^2} \lim_{\varepsilon \to 0} \left[\frac{||\vec{\hat{E}}^{meas} - \mathrm{L_E}\left(\chi_E^{(n-1)} + \varepsilon d_{E,BI}^{(n)}\right)||^2 - ||\vec{\hat{E}}^{meas} - \mathrm{L_E}\chi_E^{(n-1)}||^2}{\varepsilon} \right], \quad \text{(B.27)}$$

where ε is a real number, $d_{E,BI}^{(n)}$ is the contribution of $Err_{E,BI}^{(n)}$ to the update direction $d_E^{(n)}$ in (B.2). Following the same argument as in Section B.1.1, equation (B.27) reduces to

$$\frac{\partial Err_{E,BI}^{(n)}}{\partial \chi_E^{(n)}} = \frac{-2\mathrm{Re} < \mathrm{L_E^\dagger} r_E^{(n-1)}, d_{E,BI}^{(n)} >}{||\vec{\hat{E}}^{meas}||^2}, \quad \text{(B.28)}$$

To minimize equation (B.9), the inner product of $\mathrm{L_E^\dagger} r_E^{(n-1)}$ and $d_{E,BI}^{(n)}$ is to be maximized. Now, $\mathrm{L_E^\dagger} r_E^{(n-1)}$ and $d_{E,BI}^{(n)}$ are set parallel, to result in

$$d_{E,BI}^{(n)} = \mathrm{L_E^\dagger} r_E^{(n-1)}. \quad \text{(B.29)}$$

The minimization by means of a Fréchet derivative with respect to the electromagnetic contrast of the second term in (B.26) is written as,

$$\frac{\partial Err_{CG}^{(n)}}{\partial \chi_E^{(n)}} = \frac{\beta_E}{||\nabla\chi_A^{(n-1)} \times \nabla\chi_E^{(n-1)}||^2} \lim_{\varepsilon \to 0} \left[\frac{||\nabla\chi_A^{(n)} \times \nabla\left(\chi_E^{(n-1)} + \varepsilon d_{E,CG}^{(n)}\right)||^2 - ||\nabla\chi_A^{(n)} \times \nabla\chi_E^{(n-1)}||^2}{\varepsilon} \right], \quad \text{(B.30)}$$

where $d_{E,CG}^{(n)}$ is the contribution of $Err_{E,CG}^{(n)}$ to the update direction $d_E^{(n)}$. By expanding the brackets, expanding the square terms and taking the limit of $\varepsilon \to 0$, similar to the steps for the acoustic case in equations (B.12 - B.15),

$$\frac{\partial Err_{E,CG}^{(n)}}{\partial \chi_E^{(n)}} = \frac{2\beta_E \mathrm{Re} < \nabla\chi_E^{(n-1)} \times \nabla d_{E,CG}^{(n)}, \nabla\chi_A^{(n)} \times \nabla\chi_E^{(n-1)} >}{||\nabla\chi_A^{(n-1)} \times \nabla\chi_E^{(n-1)}||^2} \quad \text{(B.31)}$$

$$= \frac{2\beta_E \mathrm{Re} < \vec{a}^{(n)} \times \nabla d^{(n)}, \vec{b}^{(n)} >}{||\vec{b}^{(n-1)}||^2}, \quad \text{(B.32)}$$

is obtained. In (B.32) $d^{(n)} = d_{E,CG}^{(n)}$, $\vec{a}^{(n)} = \nabla\chi_A^{(n)}$, $\vec{b}^{(n)} = \nabla\chi_A^{(n)} \times \nabla\chi_E^{(n-1)}$ and $\vec{b}^{(n-1)} = \nabla\chi_A^{(n-1)} \times \nabla\chi_E^{(n-1)}$ are used for simplification of the notation. Next, equation (B.32) is written in the integral form, and a circular shift is applied to the triple product inside of the integral, $\vec{A}\cdot(\vec{B}\times\vec{C}) = \vec{B}\cdot(\vec{C}\times\vec{A})$. After that the vector calculus identity $(\nabla\phi)\times\vec{A} = \nabla\times(\phi\vec{A}) - \phi(\nabla\times\vec{A})$ is used to result in,

$$\frac{\partial Err_{E,CG}^{(n)}}{\partial\chi_E^{(n)}} = \frac{2\beta_E}{||\vec{b}^{(n-1)}||^2}\mathrm{Re}\int_V \left(\nabla d^{(n)}\times\vec{b}^{(n)*}\right)\cdot\vec{a}^{(n)}dV \tag{B.33}$$

$$= \frac{2\beta_E}{||\vec{b}^{(n-1)}||^2}\mathrm{Re}\int_V \left(\nabla\times\left(d^{(n)}\vec{b}^{(n)*}\right)\right)\cdot\vec{a}^{(n)} - d^{(n)}\left(\nabla\times\vec{b}^{(n)*}\right)\cdot\vec{a}^{(n)}dV. \tag{B.34}$$

Now on the first term in equation (B.34) the vector calculus identity $\nabla\cdot(\vec{A}\times\vec{B}) = (\nabla\times\vec{A})\cdot\vec{B} - (\nabla\times\vec{B})\cdot\vec{A}$ and subsequently Gauss' theorem is applied to the first term,

$$\frac{\partial Err_{E,CG}^{(n)}}{\partial\chi_E^{(n)}} = \frac{2\beta_E}{||\vec{b}^{(n-1)}||^2}\mathrm{Re}\int_V \nabla\cdot\left(d^{(n)}\vec{b}^{(n)*}\times\vec{a}^{(n)}\right) + \left(\nabla\times\vec{a}^{(n)}\right)\cdot d^{(n)}\vec{b}^{(n)*} - d^{(n)}\left(\nabla\times\vec{b}^{(n)*}\right)\cdot\vec{a}^{(n)}dV \tag{B.35}$$

$$= \frac{2\beta_E}{||\vec{b}^{(n-1)}||^2}\mathrm{Re}\left[\int_{\partial V} d^{(n)}\vec{b}^{(n)*}\times\vec{a}^{(n)}dS + \int_V d^{(n)}\left(\nabla\times\vec{a}^{(n)}\right)\cdot\vec{b}^{(n)*} - d^{(n)}\left(\nabla\times\vec{b}^{(n)*}\right)\cdot\vec{a}^{(n)*}dV\right]. \tag{B.36}$$

Analogous to the acoustic derivation, all the terms within the surface integral consist of contrasts, which are assumed to be zero on the boundary. This term therefore vanishes. The remaining part reduces, using the vector calculus identity $\nabla\cdot(\vec{A}\times\vec{B}) = (\nabla\times\vec{A})\cdot\vec{B} - (\nabla\times\vec{B})\cdot\vec{A}$, to

$$\frac{\partial Err_{E,CG}^{(n)}}{\partial\chi_E^{(n)}} = \frac{-2\beta_E\mathrm{Re}\int_V d^{(n)}\nabla\cdot\left(\vec{b}^{(n)*}\times\vec{a}^{(n)}\right)dV}{||\vec{b}^{(n-1)}||^2}. \tag{B.37}$$

To minimize (B.37), $d^{(n)}$ and $\nabla\cdot\left(\vec{b}^{(n)}\times\vec{a}^{(n)*}\right)$ are set parallel to obtain,

$$d_{E,CG}^{(n)} = \nabla\cdot\left[\left(\nabla\chi_A^{(n)}\times\nabla\chi_E^{(n-1)}\right)\times\nabla\chi_A^{(n)*}\right] \tag{B.38}$$

$$= \nabla\cdot\left[\nabla\chi_A^{(n)*}\times\left(\nabla\chi_E^{(n-1)}\times\nabla\chi_A^{(n)}\right)\right]. \tag{B.39}$$

So in total, the update direction for the electromagnetic contrast is given by

$$d_E^{(n)} = d_{E,BI}^{(n)} + d_{E,CG}^{(n)} = \mathrm{L_E^\dagger} r_E^{(n-1)} + \nabla\cdot\left[\nabla\chi_A^{(n)*}\times\left(\nabla\chi_E^{(n-1)}\times\nabla\chi_A^{(n)}\right)\right]. \tag{B.40}$$

Update amplitude

To find the update amplitude of the electromagnetic contrast, $\alpha_E^{(n)}$ in equation (B.2), a similar derivation as used in the acoustic case is followed. The error function (B.26) is rewritten and subsequently minimized with respect to $\alpha_E^{(n)}$. Firstly, equation (B.2) is plugged into the error function, to obtain

$$Err_E^{(n)} = \frac{||\vec{\hat{E}}^{meas} - \mathrm{L_E}\left(\chi_E^{(n-1)} + \alpha_E^{(n)}d_E^{(n)}\right)||^2}{||\vec{\hat{E}}^{meas}||^2} + \beta_E\frac{||\nabla\chi_A^{(n)}\times\nabla\left(\chi_E^{(n-1)} + \alpha_E^{(n)}d_E^{(n)}\right)||^2}{||\nabla\chi_A^{(n-1)}\times\nabla\chi_E^{(n-1)}||^2}. \tag{B.41}$$

Next, by using the residual in (B.4) and expanding the brackets and square terms equation (B.41) becomes

$$Err_E^{(n)} = \frac{||r_E^{(n-1)}||^2 + \alpha_E^{(n)2}||\mathrm{L_E}d_E^{(n)}||^2 - 2\alpha_E^{(n)}\mathrm{Re}\,<r_E^{(n-1)}, \mathrm{L_E}d_E^{(n)}>}{||\vec{\hat{E}}^{meas}||^2} + \tag{B.42}$$

$$\beta_E\frac{||\nabla\chi_A^{(n)}\times\nabla\chi_E^{(n-1)}||^2 + \alpha_E^{(n)2}||\nabla\chi_A^{(n)}\times\nabla d_E^{(n)}||^2 + 2\alpha_E^{(n)}\mathrm{Re}<\nabla\chi_A^{(n)}\times\nabla\chi_E^{(n-1)}, \nabla\chi_A^{(n)}\times\nabla d_E^{(n)}>}{||\nabla\chi_A^{(n-1)}\times\nabla\chi_E^{(n-1)}||^2}.$$

Now, the error (B.42) is minimized with respect to $\alpha_E^{(n)}$,

$$\frac{\partial Err_E^{(n)}}{\partial \alpha_E^{(n)}} = \frac{2\alpha_E^{(n)}||\mathrm{L_E} d_E^{(n)}||^2 - 2\mathrm{Re} < r_E^{(n-1)}, \mathrm{L_E} d_E^{(n)} >}{||\vec{\hat{E}}^{meas}||^2} + \beta_E \frac{2\alpha_E^{(n)}||\nabla\chi_A^{(n)} \times \nabla d_E^{(n)}||^2 + 2\mathrm{Re} < \nabla\chi_A^{(n)} \times \nabla\chi_E^{(n-1)}, \nabla\chi_A^{(n)} \times \nabla d_E^{(n)} >}{||\nabla\chi_A^{(n-1)} \times \nabla\chi_E^{(n-1)}||^2} = 0. \tag{B.43}$$

Reordering the terms, $\alpha_E^{(n)}$ is found to be

$$\alpha_E^{(n)} = \frac{\mathrm{Re} < r_E^{(n-1)}, \mathrm{L_E} d_E^{(n)} > ||\nabla\chi_A^{(n-1)} \times \nabla\chi_E^{(n-1)}||^2 - \beta_E \mathrm{Re} < \nabla\chi_A^{(n)} \times \nabla\chi_E^{(n-1)}, \nabla\chi_A^{(n)} \times \nabla d_E^{(n)} > ||\vec{\hat{E}}^{meas}||^2}{||\mathrm{L_E} d_E^{(n)}||^2 ||\nabla\chi_A^{(n-1)} \times \nabla\chi_E^{(n-1)}||^2 + \beta_E ||\nabla\chi_A^{(n)} \times \nabla d_E^{(n)}||^2 ||\vec{\hat{E}}^{meas}||^2}. \tag{B.44}$$

B.2. Gradient difference approach

This section holds the derivation of the update direction and amplitude, when using the GD constraint. In the developed algorithm, the acoustic contrast will be updated first, followed by the electromagnetic contrast. Therefore, the electromagnetic derivation will follow after the acoustic derivation of the update parameters.

B.2.1. Acoustic field

The error function to be minimized when using the difference in normalized contrast gradients as the structural constraint at the n-th iteration is

$$Err_A^{(n)} = Err_{A,BI}^{(n)} + Err_{A,GD}^{(n)} = \frac{||\hat{p}^{meas} - \mathrm{L_A}\chi_A^{(n)}||^2}{||\hat{p}^{meas}||^2} + \beta_A ||\nabla\overline{\chi}_A^{(n)} - \nabla\overline{\chi}_E^{(n-1)}||^2, \tag{B.45}$$

where $Err_{A,GD}^{(n)}$ is the contribution to the total error due to the joint structural constraint by the difference in contrast gradients. The location dependencies of $\hat{p}^{meas}$, χ_A and χ_E are left out for simplicity. Note that in the $Err_{A,GD}^{(n)}$-term, the electromagnetic contrast of the $(n-1)$-th iteration is used, as the acoustic contrast is updated before the electromagnetic contrast. In (B.45), $\overline{\chi}_A^{(n)}$ and $\overline{\chi}_E^{(n)}$ are the normalized contrasts of the acoustic and electromagnetic field at the n-th iteration, and are defined as

$$\overline{\chi}_A^{(n)} = \frac{\chi_A^{(n)}}{\mathrm{Max}|\mathrm{Re}(\chi_A)|} = \frac{\chi_A^{(n)}}{\chi_{A,Max}^{(n)}}, \tag{B.46}$$

$$\overline{\chi}_E^{(n)} = \frac{\chi_E^{(n)}}{\mathrm{Max}|\mathrm{Re}(\chi_E)|} = \frac{\chi_E^{(n)}}{\chi_{E,Max}^{(n)}}. \tag{B.47}$$

Update direction

The steepest negative direction of error function (B.45) is found using a Fréchet derivative. The update direction for the term $Err_{A,BI}^{(n)}$ is identical to the earlier derivation with the result given in equation (B.10). The Fréchet derivative of the second term on the right-hand side in (B.45) is given by

$$\frac{\partial Err_{GD}^{(n)}}{\partial \chi_A^{(n)}} = \beta_A \lim_{\varepsilon \to 0} \frac{1}{\varepsilon} \left[||\nabla \left(\frac{\chi_A^{(n-1)} + \varepsilon d_{A,GD}^{(n)}}{\chi_{A,Max}^{(n-1)}} \right) - \nabla\overline{\chi}_E^{(n-1)}||^2 - ||\nabla\overline{\chi}_A^{(n-1)} - \nabla\overline{\chi}_E^{(n-1)}||^2 \right], \tag{B.48}$$

where ε is a small, real number, $d_{A,GD}^{(n)}$ is the contribution of $Err_{A,GD}^{(n)}$ to the update direction $d_A^{(n)}$ in (B.1) and $\chi_{A,Max}^{(n-1)}$ is the maximum of the absolute value of the real part of the acoustic contrast at the n-th iteration. By expanding the brackets, expanding the square terms and taking the limit of $\varepsilon \to 0$, equation

(B.48) is reduced to

$$\frac{\partial Err_{A,GD}^{(n)}}{\partial \chi_A^{(n)}} = \beta_A \lim_{\varepsilon \to 0} \frac{1}{\varepsilon} \left[||\nabla \overline{\chi}_A^{(n-1)} - \nabla \overline{\chi}_E^{(n-1)} + \frac{\varepsilon}{\chi_{A,Max}^{(n-1)}} \nabla d_{A,GD}^{(n)}||^2 - ||\nabla \overline{\chi}_A^{(n-1)} - \nabla \overline{\chi}_E^{(n-1)}||^2 \right] \quad \text{(B.49)}$$

$$= \beta_A \lim_{\varepsilon \to 0} \left[\frac{\varepsilon}{\left(\chi_{A,Max}^{(n-1)}\right)^2} ||\nabla d_{A,GD}^{(n)}||^2 - \frac{2}{\chi_{A,Max}^{(n-1)}} \mathrm{Re} < \nabla \overline{\chi}_E^{(n-1)} - \nabla \overline{\chi}_A^{(n-1)}, \nabla d_{A,GD}^{(n)} > \right] \quad \text{(B.50)}$$

$$= -\frac{2\,\beta_A}{\chi_{A,Max}^{(n-1)}} \mathrm{Re} < \nabla(\overline{\chi}_E^{(n-1)} - \overline{\chi}_A^{(n-1)}), \nabla d_{A,GD}^{(n)} > . \quad \text{(B.51)}$$

Since the goal is to find $d_{A,GD}$, and the gradient of it, the inner product of the discrete gradients requires some further inspection. The vectors within the inner product in (B.51) have a dimension of 2 x N_x x N_y with N_x and N_y the number of discrete steps of the domain in the x- and y-direction respectively. This inner product can be rewritten into the sum of two (N_x,N_y)-dimensional inner products as follows

$$< \nabla a, \nabla d > = < \frac{\partial a}{\partial x}, \frac{\partial d}{\partial x} > + < \frac{\partial a}{\partial y}, \frac{\partial d}{\partial y} >, \quad \text{(B.52)}$$

where the notation $a = \overline{\chi}_E^{(n-1)} - \overline{\chi}_A^{(n-1)}$ and $d = d_{A,GD}^{(n)}$ is used. In this thesis, the central difference is used for the discrete differentials. The first term in (B.52) is therefore written in discrete form as

$$\frac{1}{2\Delta x} < a_{i+1,j} - a_{i-1,j},\, d_{i+1,j} - d_{i-1,j} > = \frac{1}{2\Delta x} \left[< a_{i+1,j} - a_{i-1,j},\, d_{i+1,j} > - < a_{i+1,j} - a_{i-1,j},\, d_{i-1,j} > \right], \quad \text{(B.53)}$$

where Δx is the spatial spacing of the domain, i the index for the x-direction and j the index for the y-direction. Now when disregarding the first two and the last two rows the vectors, the two terms on the right-hand side of (B.53) can be recombined to yield

$$\frac{1}{2\Delta x} \left[< 2a_{i,j} - a_{i-2,j} - a_{i+2,j},\, d_{i,j} > \right]. \quad \text{(B.54)}$$

The same procedure can be done for the derivative in the y-direction, to give

$$\frac{1}{2\Delta x} \left[< 2a_{i,j} - a_{i,j-2} - a_{i,j+2},\, d_{i,j} > \right]. \quad \text{(B.55)}$$

Summing (B.54) and (B.55), not including the outer two rows and columns of the vectors, the final discrete inner product is obtained

$$\frac{1}{2\Delta x} [< 4a_{i,j} - a_{i-2,j} - a_{i+2,j} - a_{i,j-2} - a_{i,j+2},\, d_{i,j} >], \quad \text{(B.56)}$$

where the left side of the inner product can be recognized as the discrete negative Laplacian. Therefore (B.51) can be rewritten as

$$\frac{\partial Err_{A,GD}^{(n)}}{\partial \chi_A^{(n)}} = -\frac{2\,\beta_A}{\chi_{A,Max}^{(n-1)}} \mathrm{Re} < \nabla^2 \left(\overline{\chi}_A^{(n-1)} - \overline{\chi}_E^{(n-1)} \right), d_{A,GD}^{(n)} > . \quad \text{(B.57)}$$

To minimize this result, $\nabla^2(\overline{\chi}_A^{(n-1)} - \overline{\chi}_E^{(n-1)})^*$ should be parallel to $d_{A,GD}^{(n)}$, to give[1]

$$d_{A,GD}^{(n)} = \nabla^2 \left(\overline{\chi}_A^{(n-1)} - \overline{\chi}_E^{(n-1)} \right)^* . \quad \text{(B.58)}$$

In total, the update direction for the acoustic contrast when using the difference method is

$$d_A^{(n)} = d_{A,BI}^{(n)} + d_{A,GD}^{(n)} = \mathrm{L_A^\dagger} r_A^{(n-1)} + \nabla^2 \left(\overline{\chi}_A^{(n-1)} - \overline{\chi}_E^{(n-1)} \right)^* . \quad \text{(B.59)}$$

[1] Inspection of the simulated $d_{A,GD}^{(n)}$ has shown an extra minus sign is required in front of equation (B.58), for the update direction to be correct. It is unclear whether there exists a flaw in the derivation, or in the implemented code.

Update amplitude

To find the update amplitude of the acoustic contrast, $\alpha_A^{(n)}$ in equation (B.1), error function (B.45) is minimized with respect to $\alpha_A^{(n)}$. In order to do this, the error function first needs to be rewritten, starting by plugging in equation (B.1), to obtain

$$Err_A^{(n)} = \frac{||\hat{p}^{meas} - \mathrm{L_A}\left(\chi_A^{(n-1)} + \alpha_A^{(n)} d_A^{(n)}\right)||^2}{||\hat{p}^{meas}||^2} + \beta_A ||\nabla\left(\frac{\chi_A^{(n-1)} + \alpha_A^{(n)} d_A^{(n)}}{\chi_{A,Max}^{(n-1)}}\right) - \nabla\overline{\chi}_E^{(n-1)}||^2. \tag{B.60}$$

Next, by expanding the brackets and square terms and using the residual in (B.3), equation (B.60) becomes

$$Err_A^{(n)} = \frac{||r_A^{(n-1)}||^2 + \alpha_A^{(n)2}||\mathrm{L_A} d_A^{(n)}||^2 - 2\alpha_A^{(n)}\mathrm{Re} < r_A^{(n-1)}, \mathrm{L_A} d_A^{(n)} >}{||\hat{p}^{meas}||^2} + \tag{B.61}$$

$$\beta_A ||\nabla\overline{\chi}_A^{(n-1)} - \nabla\overline{\chi}_E^{(n-1)}||^2 + \frac{\beta_A \alpha_A^{(n)2}}{\left(\chi_{A,Max}^{(n-1)}\right)^2}||\nabla d_A^{(n)}||^2 + \frac{2\beta_A \alpha_A^{(n)}}{\chi_{A,Max}^{(n-1)}}\mathrm{Re} < \nabla\overline{\chi}_A^{(n-1)} - \nabla\overline{\chi}_E^{(n-1)}, \nabla d_A^{(n)} >.$$

Now, the error (B.62) is minimized with respect to $\alpha_A^{(n)}$,

$$\frac{\partial Err_A^{(n)}}{\partial \alpha_A^{(n)}} = \frac{2\alpha_A^{(n)}||\mathrm{L_A} d_A^{(n)}||^2 - 2\mathrm{Re} < r_A^{(n-1)}, \mathrm{L_A} d_A^{(n)} >}{||\hat{p}^{meas}||^2} +$$

$$\frac{2\beta_A \alpha_A^{(n)}}{\left(\chi_{A,Max}^{(n-1)}\right)^2}||\nabla d_A^{(n)}||^2 + \frac{2\beta_A}{\chi_{A,Max}^{(n-1)}}\mathrm{Re} < \nabla\overline{\chi}_A^{(n-1)} - \nabla\overline{\chi}_E^{(n-1)}, \nabla d_A^{(n)} >= 0. \tag{B.62}$$

Reordering the terms, $\alpha_A^{(n)}$ is found to be

$$\alpha_A^{(n)} = \frac{\mathrm{Re} < r_A^{(n-1)}, \mathrm{L_A} d_A^{(n)} > - \frac{\beta_A}{\chi_{A,Max}^{(n-1)}}\mathrm{Re} < \nabla\overline{\chi}_A^{(n-1)} - \nabla\overline{\chi}_E^{(n-1)}, \nabla d_A^{(n)} > ||\hat{p}^{meas}||^2}{||\mathrm{L_A} d_A^{(n)}||^2 + \frac{\beta_A}{\left(\chi_{A,Max}^{(n-1)}\right)^2}||\nabla d_A^{(n)}||^2 ||\hat{p}^{meas}||^2}. \tag{B.63}$$

B.2.2. Electromagnetic field

The error function for the electromagnetic contrast to be minimized when using the difference in contrasts as the structural constraint at the n-th iteration is

$$Err_E^{(n)} = Err_{E,BI}^{(n)} + Err_{E,GD}^{(n)} = \frac{||\vec{\hat{E}}^{\,meas} - \mathrm{L_E}\chi_E^{(n)}||^2}{||\vec{\hat{E}}^{\,meas}||^2} + \beta_E ||\nabla\overline{\chi}_A^{(n)} - \nabla\overline{\chi}_E^{(n)}||^2, \tag{B.64}$$

where $Err_{E,GD}^{(n)}$ is the contribution to the total error due to the GD constraint for the electromagnetic case and the location dependencies of $\vec{\hat{E}}^{\,meas}$, χ_A and χ_E are left out for simplicity. Note that in the electromagnetic case, within the $Err_{E,GD}^{(n)}$-term, the acoustic contrast of the n-th iteration is used, since it was updated before the electromagnetic contrast within the same iteration.

Update direction

The update direction for term $Err_{E,BI}^{(n)}$ is identical to the earlier derivation with the result given in equation (B.29). The Fréchet derivative of the second term in error function (B.64) can be written as

$$\frac{\partial Err_{E,GD}^{(n)}}{\partial \chi_E^{(n)}} = \beta_E \lim_{\varepsilon \to 0} \frac{1}{\varepsilon}\left[||\nabla\overline{\chi}_A^{(n)} - \nabla\left(\frac{\chi_E^{(n-1)} + \varepsilon d_{E,GD}^{(n)}}{\chi_{E,Max}^{(n-1)}}\right)||^2 - ||\nabla\overline{\chi}_A^{(n)} - \nabla\overline{\chi}_E^{(n-1)}||^2\right], \tag{B.65}$$

where ε is a small, real number and $d_{E,GD}^{(n)}$ is the contribution of $Err_{E,GD}^{(n)}$ to the update direction $d_E^{(n)}$ in (B.2), and $\chi_{E,Max}^{(n)}$ is the maximum value of the absolute value of the real part of the electromagnetic

contrast at the n-the iteration. By expanding the brackets, expanding the square terms and taking the limit of $\varepsilon \to 0$, equation (B.30) is reduced to

$$\frac{\partial Err_{E,GD}^{(n)}}{\partial \chi_E^{(n)}} = \beta_E \lim_{\varepsilon\to 0} \frac{1}{\varepsilon}\left[||\nabla \overline{\chi}_A^{(n)} - \nabla \overline{\chi}_E^{(n-1)} - \frac{\varepsilon}{\chi_{E,Max}^{(n-1)}}\nabla d_{E,GD}^{(n)}||^2 - ||\nabla \overline{\chi}_A^{(n)} - \nabla \overline{\chi}_E^{(n-1)}||^2\right] \tag{B.66}$$

$$= \beta_E \lim_{\varepsilon\to 0}\left[\frac{\varepsilon}{\left(\chi_{E,Max}^{(n-1)}\right)^2}||\nabla d_{E,GD}^{(n)}||^2 - \frac{2}{\chi_{E,Max}^{(n-1)}}\mathrm{Re} < \nabla \overline{\chi}_A^{(n)} - \nabla \overline{\chi}_E^{(n-1)}, \nabla d_{E,GD}^{(n)} >\right] \tag{B.67}$$

$$= -\frac{2\,\beta_E}{\chi_{E,Max}^{(n-1)}}\,\mathrm{Re} < \nabla\left(\overline{\chi}_A^{(n)} - \overline{\chi}_E^{(n-1)}\right), \nabla d_{E,GD}^{(n)} > . \tag{B.68}$$

Following the same steps as in the acoustic case in equations (B.52 - B.56), again the inner product in equation (B.68), can be rewritten as

$$\frac{\partial Err_{E,GD}^{(n)}}{\partial \chi_E^{(n)}} = -\frac{2\,\beta_E}{\chi_{E,Max}^{(n-1)}}\,\mathrm{Re} < -\nabla^2\left(\overline{\chi}_A^{(n)} - \overline{\chi}_E^{(n-1)}\right), d_{E,GD}^{(n)} > . \tag{B.69}$$

To minimize this result, $\nabla^2\left(\chi_A^{(n)} - \chi_E^{(n-1)}\right)^*$ should be parallel to $\nabla d_{E,GD}^{(n)}$, to give

$$d_{E,GD}^{(n)} = \nabla^2\left(\overline{\chi}_E^{(n-1)} - \overline{\chi}_A^{(n)}\right)^* . \tag{B.70}$$

In total, the update direction for the acoustic contrast when using the difference method is

$$d_E^{(n)} = d_{E,BI}^{(n)} + d_{E,GD}^{(n)} = \mathrm{L}_\mathrm{E}^\dagger r_E^{(n-1)} + \nabla^2\left(\overline{\chi}_E^{(n-1)} - \overline{\chi}_A^{(n)}\right)^* . \tag{B.71}$$

Update amplitude

To find the update amplitude of the electromagnetic contrast, $\alpha_E^{(n)}$ in equation (B.2), once again error function (B.45) is minimized with respect to $\alpha_E^{(n)}$. To start, the error function first is rewritten by plugging in equation (B.2), to obtain

$$Err_E^{(n)} = \frac{||\vec{\hat{E}}^{\,meas} - \mathrm{L_E}\left(\chi_E^{(n-1)} + \alpha_E^{(n)} d_E^{(n)}\right)||^2}{||\vec{\hat{E}}^{\,meas}||^2} + \beta_E||\nabla\chi_A^{(n)} - \left(\frac{\nabla(\chi_E^{(n-1)} + \alpha_E^{(n)} d_E^{(n)})}{\chi_{E,Max}^{(n-1)}}\right)||^2. \tag{B.72}$$

Next, by expanding the brackets and square terms and using the residual in (B.4), equation (B.72) becomes

$$Err_E^{(n)} = \frac{||r_E^{(n-1)}||^2 + \alpha_E^{(n)2}||\mathrm{L_E} d_E^{(n)}||^2 - 2\alpha_E^{(n)}\mathrm{Re}\ < r_E^{(n-1)}, \mathrm{L_E} d_E^{(n)} >}{||\vec{\hat{E}}^{\,meas}||^2} + \tag{B.73}$$

$$\beta_E||\nabla \overline{\chi}_A^{(n)} - \nabla \overline{\chi}_E^{(n-1)}||^2 + \frac{\beta_E \alpha_E^{(n)2}}{\left(\chi_{E,Max}^{(n-1)}\right)^2}||\nabla d_E^{(n)}||^2 - \frac{2\beta_E \alpha_E^{(n)}}{\chi_{E,Max}^{(n-1)}}\mathrm{Re}\ < \nabla \overline{\chi}_A^{(n)} - \nabla \overline{\chi}_E^{(n-1)}, \nabla d_E^{(n)} > .$$

Now, the error (B.74) is minimized with respect to $\alpha_E^{(n)}$,

$$\frac{\partial Err_E^{(n)}}{\partial \alpha_E^{(n)}} = \frac{2\alpha_E^{(n)}||\mathrm{L_E} d_E^{(n)}||^2 - 2\mathrm{Re} < r_E^{(n-1)}, \mathrm{L_E} d_E^{(n)} >}{||\vec{\hat{E}}^{\,meas}||^2} +$$

$$\frac{2\beta_E \alpha_E^{(n)}}{\left(\chi_{E,Max}^{(n-1)}\right)^2}||\nabla d_E^{(n)}||^2 - \frac{2\beta_E}{\chi_{E,Max}^{(n-1)}}\mathrm{Re}\ < \nabla \overline{\chi}_A^{(n)} - \nabla \overline{\chi}_E^{(n-1)}, \nabla d_E^{(n)} >= 0. \tag{B.74}$$

Reordering the terms, $\alpha_E^{(n)}$ is found to be

$$\alpha_E^{(n)} = \frac{\mathrm{Re} < r_E^{(n-1)}, \mathrm{L_E} d_E^{(n)} > + \frac{\beta_E}{\chi_{E,Max}^{(n-1)}}\mathrm{Re}\ < \nabla \overline{\chi}_A^{(n)} - \nabla \overline{\chi}_E^{(n-1)}, \nabla d_E^{(n)} > ||\vec{\hat{E}}^{\,meas}||^2}{||\mathrm{L_E} d_E^{(n)}||^2 + \frac{\beta_E}{\left(\chi_{E,Max}^{(n-1)}\right)^2}||\nabla d_E^{(n)}||^2||\vec{\hat{E}}^{\,meas}||^2}. \tag{B.75}$$

Bibliography

[1] R. G. Maev, R. Green Jr, and A. Siddiolo, "Review of advanced acoustical imaging techniques for nondestructive evaluation of art objects," *Research in Nondestructive Evaluation*, vol. 17, no. 4, pp. 191–204, 2006.

[2] T. Hopp, N. Ruiter, J. C. Bamber, N. Duric, and K. W. A. van Dongen, *Proceedings of the International Workshop on Medical Ultrasound Tomography: 1.-3. Nov. 2017, Speyer, Germany*. KIT Scientific Publishing, 2018.

[3] D. R. Dowling and K. G. Sabra, "Acoustic remote sensing," *Annual Review of Fluid Mechanics*, vol. 47, pp. 221–243, 2015.

[4] C. Hübscher and K. Gohl, "Reflection/refraction seismology," in *(Encyclopedia of Earth Sciences Series)*, pp. 721–731, Springer, 2016.

[5] U. Hasar, "Non-destructive testing of hardened cement specimens at microwave frequencies using a simple free-space method.," *NDT & E International*, vol. 42, no. 6, pp. 550–557, 2009.

[6] R. Chandra, H. Zhou, I. Balasingham, and R. M. Narayanan, "On the opportunities and challenges in microwave medical sensing and imaging," *IEEE Transactions on Biomedical Engineering*, vol. 62, no. 7, pp. 1667–1682, 2015.

[7] A. Jordan and M. Veysoglu, "Electromagnetic remote sensing of sea ice," *Inverse Problems*, vol. 10, no. 5, p. 1041, 1994.

[8] F. Li, Q. Liu, and L. Song, "Three-dimensional reconstruction of objects buried in layered media using born and distorted born iterative methods," *IEEE Geosicience and Remote Sensing Letters*, vol. 1, no. 2, pp. 107–111, 2004.

[9] A. Abubakar, T. Habashy, M. Li, and J. Liu, "Inversion algorithms for large-scale geophysical electromagnetic measurements.," *Inverse Problems*, vol. 25, no. 12, p. 123012, 2009.

[10] W. Hu, A. Abubakar, and T. M. Habashy, "Joint electromagnetic and seismic inversion using structural constraints," *Geophysics*, vol. 74, no. 6, pp. R99–R109, 2009.

[11] P. Harris and L. MacGregor, "Determination of reservoir properties from the integration of csem, seismic, and well-log data," *First Break*, vol. 24, no. 11, 2006.

[12] M. Omer, P. Mojabi, D. Kurrant, J. LoVetri, and E. Fear, "Proof-of-concept of the incorporation of ultrasound-derived structural information into microwave radar imaging," *IEEE Journal on Multiscale and Multiphysics Computational Techniques*, vol. 3, pp. 129–139, 2018.

[13] Y. Qin, T. Rodet, M. Lambert, and D. Lesselier, "Joint inversion of electromagnetic and acoustic data with edge-preserving regularization for breast imaging," *IEEE Transactions on Computational Imaging*, vol. 7, pp. 349–360, 2021.

[14] L. Chandrashekar and A. Sreedevi, "Advances in biomedical imaging and image fusion," *International Journal of Computer Applications*, vol. 179, no. 24, pp. 1–9, 2018.

[15] N. Abdollahi, D. Kurrant, P. Mojabi, M. Omer, E. Fear, and J. LoVetri, "Incorporation of ultrasonic prior information for improving quantitative microwave imaging of breast," *IEEE Journal on Multiscale and Multiphysics Computational Techniques*, vol. 4, pp. 98–110, 2019.

[16] N. Bayat, P. Mojabi, J. LoVetri, and P. Mojabi, "On microwave breast imaging with ultrasound spatial priors," in *2020 XXXIIIrd General Assembly and Scientific Symposium of the International Union of Radio Science*, pp. 1–4, IEEE, 2020.

[17] Y. Qin, T. Rodet, M. Lambert, and D. Lesselier, “Microwave breast imaging with prior ultrasound information,” *IEEE Open Journal of Antennas and Propagation*, vol. 1, pp. 472–482, 2020.

[18] P. Mojabi, M. Hughson, V. Khoshdel, I. Jeffrey, and J. Lovetri, “CNN for compressibility to permittivity mapping for combined ultrasound-microwave breast imaging,” *IEEE Journal on Multiscale and Multiphysics Computational Techniques*, vol. 6, pp. 62–72, 2021.

[19] Y. Qin, Y. Zhang, Q. Zhao, Z. Zhao, and Z. Nie, “Joint inversion of electromagnetic and acoustic data with spatial-constrained by fcm,” in *2021 IEEE 4th International Conference on Electronics Technology (ICET)*, pp. 213–216, IEEE, 2021.

[20] Y. M. Wang and W. C. Chew, “An iterative solution of the two-dimensional electromagnetic inverse scattering problem,” *International Journal of Imaging Systems and Technology*, vol. 1, no. 1, pp. 100–108, 1989.

[21] W. C. Chew and Y. M. Wang, “Reconstruction of two-dimensional permittivity distribution using the distorted born iterative method,” *IEEE Transactions on Medical Imaging*, vol. 9, no. 2, pp. 218–225, 1990.

[22] N. Zaiping, Y. Feng, Z. Yanwen, and Z. Yerong, “Variational born iteration method and its applications to hybrid inversion,” *IEEE Transactions on Geoscience and Remote Sensing*, vol. 38, no. 4, pp. 1709–1715, 2000.

[23] A. Abubakar, P. M. van den Berg, and S. Y. Semenov, “A robust iterative method for born inversion,” *IEEE Transactions on Geoscience and Remote Sensing*, vol. 42, no. 2, pp. 342–354, 2004.

[24] P. M. van den Berg, A. van Broekhoven, and A. Abubakar, “Extended contrast source inversion,” *Inverse Problems*, vol. 15, no. 5, p. 1325, 1999.

[25] X. Chen, “Subspace-based optimization method for solving inverse-scattering problems,” *IEEE Transactions on Geoscience and Remote Sensing*, vol. 48, no. 1, pp. 42–49, 2009.

[26] E. Haber and M. H. Gazit, “Model fusion and joint inversion,” *Surveys in Geophysics*, vol. 34, no. 5, pp. 675–695, 2013.

[27] G. M. Hoversten, F. Cassassuce, E. Gasperikova, G. A. Newman, J. Chen, Y. Rubin, Z. Hou, and D. Vasco, “Direct reservoir parameter estimation using joint inversion of marine seismic ava and csem data,” *Geophysics*, vol. 71, no. 3, pp. C1–C13, 2006.

[28] P. Dell’Aversana, G. Bernasconi, F. Miotti, and D. Rovetta, “Joint inversion of rock properties from sonic, resistivity and density well-log measurements,” *Geophysical Prospecting*, vol. 59, no. Advances in Electromagnetic, Gravity and Magnetic Methods for Exploration, pp. 1144–1154, 2011.

[29] G. Gao, A. Abubakar, and T. M. Habashy, “Joint petrophysical inversion of electromagnetic and full-waveform seismic data,” *Geophysics*, vol. 77, no. 3, pp. WA3–WA18, 2012.

[30] T. Lan, N. Liu, F. Han, and Q. H. Liu, “Joint petrophysical and structural inversion of electromagnetic and seismic data based on volume integral equation method,” *IEEE Transactions on Geoscience and Remote Sensing*, vol. 57, no. 4, pp. 2075–2086, 2018.

[31] A. Abubakar, G. Gao, T. M. Habashy, and J. Liu, “Joint inversion approaches for geophysical electromagnetic and elastic full-waveform data,” *Inverse Problems*, vol. 28, no. 5, p. 055016, 2012.

[32] G. E. Archie, “The electrical resistivity log as an aid in determining some reservoir characteristics,” *Transactions of the AIME*, vol. 146, no. 01, pp. 54–62, 1942.

[33] F. Gassmann, “Elasticity of porous media,” *Vierteljahrsschrder Naturforschenden Gesselschaft*, vol. 96, no. 1–23, 1951.

[34] X. Song, M. Li, F. Yang, S. Xu, and A. Abubakar, “Three-dimensional joint inversion of em and acoustic data based on contrast source inversion,” *IEEE Journal on Multiscale and Multiphysics Computational Techniques*, vol. 5, pp. 28–36, 2020.

[35] E. Haber and D. Oldenburg, “Joint inversion: a structural approach,” *Inverse Problems*, vol. 13, no. 1, p. 63, 1997.

[36] L. A. Gallardo and M. A. Meju, “Characterization of heterogeneous near-surface materials by joint 2d inversion of dc resistivity and seismic data,” *Geophysical Research Letters*, vol. 30, no. 13, 2003.

[37] L. A. Gallardo and M. A. Meju, “Joint two-dimensional dc resistivity and seismic travel time inversion with cross-gradients constraints,” *Journal of Geophysical Research: Solid Earth*, vol. 109, no. B3, 2004.

[38] L. A. Gallardo, “Multiple cross-gradient joint inversion for geospectral imaging,” *Geophysical Research Letters*, vol. 34, no. 19, 2007.

[39] N. L. Bennington, H. Zhang, C. H. Thurber, and P. A. Bedrosian, “Joint inversion of seismic and magnetotelluric data in the parkfield region of california using the normalized cross-gradient constraint,” *Pure and Applied Geophysics*, vol. 172, no. 5, pp. 1033–1052, 2015.

[40] T. Lan, H. Liu, N. Liu, J. Li, F. Han, and Q. H. Liu, “Joint inversion of electromagnetic and seismic data based on structural constraints using variational born iteration method,” *IEEE Transactions on Geoscience and Remote Sensing*, vol. 56, no. 1, pp. 436–445, 2017.

[41] O. Ozdemir, A. Oncu, and K. W. A. Van Dongen, “A joint inversion method for breast imaging using electromagnetic and acoustics waves,” in *2018 International Conference on Electromagnetics in Advanced Applications (ICEAA)*, pp. 182–184, IEEE, 2018.

[42] Y. Zhang, Z. Zhao, Z. Nie, and Q. H. Liu, “Approach on joint inversion of electromagnetic and acoustic data based on structural constraints,” *IEEE Transactions on Geoscience and Remote Sensing*, vol. 58, no. 11, pp. 7672–7681, 2020.

[43] Q. Zhao, Y. Zhang, Y. Qin, Z. Zhao, and Z. Nie, “Joint inversion of electromagnetic and acoustic data based on structural constraints with te illumination,” in *2021 IEEE 4th International Conference on Electronics Technology (ICET)*, pp. 247–251, IEEE, 2021.

[44] X. Song, M. Li, F. Yang, S. Xu, and A. Abubakar, “Study on joint inversion algorithm of acoustic and electromagnetic data in biomedical imaging,” *IEEE Journal on Multiscale and Multiphysics Computational Techniques*, vol. 4, pp. 2–11, 2019.

[45] J. M. Jin, *Theory and Computation of Electromagnetic Fields*. IEEE Press John Wiley & Sons, second ed., 2015.

[46] W. C. Gibson, *The Method of Moments in Electromagnetics*. Taylor & Francis Group, 2008.

[47] A. T. de Hoop, *Handbook of Radiations and Scattering of Waves: Acoustic Waves in Fluids, Elastic Waves in Solids, Electromagnetic Waves.* Academic Press, 1995.

[48] E. G. Williams, *Fourier Acoustics, Chapter 8 - Green Functions and the Helmholtz Integral Equation*. Academic Press, 1999.

[49] N. Joachimowicz, C. Pichot, and J. P. Hugonin, “Inverse scattering: An iterative numerical method for electromagnetic imaging,” *IEEE Transactions on Antennas and Propagation*, vol. 39, no. 12, pp. 1742–1753, 1991.

[50] D. Boito, L. de Andrade, G. d. Sousa, R. Gama, and C. London, “On maxwell’s electrodynamics in two spatial dimensions,” *Revista Brasileira de Ensino de Física*, vol. 42, 2020.

[51] K. T. McDonald, *Electrodynamics in 1 and 2 spatial dimensions*. Princeton University, Princeton, NJ, September, 2014.

[52] P. M. Van Den Berg and R. E. Kleinman, “A contrast source inversion method,” *Inverse Problems*, vol. 13, no. 6, p. 1607, 1997.

[53] N. Ozmen, R. Dapp, M. Zapf, H. Gemmeke, N. V. Ruiter, and K. W. A. van Dongen, “Comparing different ultrasound imaging methods for breast cancer detection,” *IEEE Transactions on Ultrasonics, Ferroelectrics, and Frequency Control*, vol. 62, no. 4, pp. 637–646, 2015.

[54] I. Gradshteyn and I. Ryzhik, *Table of Integrals, Series and Products*. Academic Press, seventh ed., 2007. p. 915, 8.421(11).